ANKARA YILDIRIM BEYAZIT UNIVERSITY

GRADUATE SCHOOL OF NATURAL AND APPLIED SCIENCE



FABRICATION OF MULTILAYER DYE-SENSITIZED SOLAR CELLS

M. Sc. Thesis by

Aycan ATLI

Department of Energy Systems Engineering

January, 2018

ANKARA

FABRICATION OF MULTILAYER DYE-SENSITIZED SOLAR CELLS

A Thesis Submitted to
The Graduate School of Natural and Applied Sciences of
Ankara Yıldırım Beyazıt University
In Partial Fulfillment of the Requirements for the Degree of Master of Science
in Energy Systems Engineering

by

Aycan ATLI

January, 2018

ANKARA

M.Sc. THESIS EXAMINATION RESULT FORM

We have read the thesis entitled **"FABRICATION OF MULTILAYER DYE-SENSITIZED SOLAR CELLS"** completed by **Aycan ATLI** under supervision of **Prof. Dr. Abdullah YILDIZ** and we certify that in our opinion it is fully adequate, in scope and in quality, as a thesis for the degree of Master of Science.

Prof. Dr. Abdullah YILDIZ

Supervisor

Prof. Dr. Şerafettin EREL

(Jury Member)

Prof. Dr. Tülay SERİN

(Jury Member)

Prof. Dr. Fatih V. ÇELEBİ

Director

Graduate School of Natural and Applied Sciences

ETHICAL DECLARATION

I hereby declare that, in this thesis which has been prepared in accordance with the Thesis Writing Manual of Graduate School of Natural and Applied Sciences,

- All data, information and documents are obtained in the framework of academic and ethical rules,
- All information, documents and assessments are presented in accordance with scientific ethics and morals,
- All the materials that have been utilized are fully cited and referenced,
- No change has been made on the utilized materials,
- All the works presented are original,

and in any contrary case of above statements, I accept to renounce all my legal rights.

January, 2018 Aycan ATLI

ACKNOWLEDGMENTS

I would like to extend my gratitude and many thanks Prof. Dr. Abdullah YILDIZ for his guidance, keen knowledge and patience. The door to Prof. Dr. YILDIZ's office was always open whenever I ran into a trouble spot or had a question about my research or writing. Working in his photovoltaic research group, supplied me with insights into a multidisciplinary approach, combining chemistry, physics, material science, and engineering.

In addition to my advisor, I would like to thank the rest of my thesis committee: Prof. Dr. Şerafettin EREL and Prof. Dr. Tülay SERİN for their encouragement and insightful comments.

I would like to thank Assoc. Prof. Dr. Savaş SÖNMEZOĞLU and his research group for all their help in measurements.

Further, I would also like to thank Ankara Yıldırım Beyazıt University, and specifically the Department of Material Engineering for their XRD measurement support.

I am also thankful to all of my colleagues especially Abdullah ATILGAN, Kenan ÖZEL, Mohamed SBETA and Kerem YILDIZ for their support during my thesis work.

Finally, I must express my very profound gratitude to my parents, my partner İbrahim ATLI and my lovely son for providing me with unfailing support and continuous encouragement through the process of researching and writing this thesis. This accomplishment would not have been possible without them.

Thank you.

January, 2018 Aycan ATLI

FABRICATION OF MULTILAYER DYE-SENSITIZED SOLAR CELLS

ABSTRACT

In this study, dye sensitized solar cells (DSSCs) with different photoanode structures were fabricated by applying additional titania-coating. Photoanode components of the DSSCs were obtained from P25 powder, titanium tetrachloride, and titanium tetraisopropoxide. Ruthenium-based N719 dye was used to sensitize the photoanodes. A Platinum-coated counter electrode and iodide redox electrolyte were used to complete the sandwich structure of the DSSCs. X-Ray Diffraction (XRD), Atomic Force Microscopy (AFM), UV-VIS-NIR Spectroscopy, and current-voltage measurements were carried out to determine structural, morphological, optical, and electrical properties of the DSSCs. The conversion efficiency of the DSSCs were improved by introducing multilayers to the photoanode. The best efficiency was achieved with the DSSC which consisted of multi-compact titanium dioxide layers and a post-treated top layer of titanium dioxide.

Keywords: Energy, Photovoltaics, Dye-Sensitized Solar Cells, Multilayer

ÇOK KATMANLI BOYA DUYARLI GÜNEŞ HÜCRELERİNİN FABRİKASYONU

ÖZ

Bu çalışmada, farklı foto anot yapılarına sahip olan boya duyarlı güneş pilleri (DSSC), ilave titanyum-katmanları uygulanarak üretilmiştir. Boya duyarlı güneş hücrelerinin foto anot bileşenleri P25 tozu, titanium tetraklorit, and titanyum izopropoksit ‘den elde edilmiştir. Numuneleri duyarlı hale getirmek için Rutenyum bazlı N719 boyası kullanılmıştır. Sandviç güneş pili yapısını tamamlamak için platin kaplı karşı elektrot ve iyodür redoks elektrolit kullanılmıştır. Güneş pillerinin yapısal, morfolojik, optik ve elektriksel özelliklerini belirlemek için X-Işını Kırınımı (XRD), Atomik Kuvvet Mikroskopisi (AFM), UV-VIS-NIR spektrofotometrisi ve akım-gerilim ölçümleri yapılmıştır. Güneş pillerinin dönüşüm verimliliği, foto anodun çok katmanlı yapısıyla geliştirilmiştir. En iyi verimlilik, değeri arasında çoklu kompakt bir titanyum dioksit katmanı ve ilave son iyileştirme katmanı içeren güneş hücresiyle elde edilmiştir.

Anahtar Kelimeler: Enerji, Fotovoltaik, Boya duyarlı güneş hücresi, Çok katmanlı

CONTENTS

M.Sc. THESIS EXAMINATION RESULT FORM....ii
ETHICAL DECLARATION iii
ACKNOWLEDGMENTS....iv
ABSTRACT v
ÖZ....vi
ABBREVIATIONS ix
LIST OF SYMBOLS....x
LIST OF TABLES....xi
LIST OF FIGURES....xii
READING GUIDE....xiii
CHAPTER 1 INTRODUCTION 1
CHAPTER 2 DYE-SENSITIZED SOLAR CELLS 3
2.1 Components 3
2.2 Working principles 6
2.3 Equivalent circuit 7
2.4 Losses 8
2.5 Literature Review 9
CHAPTER 3 EXPERIMENTAL WORK 11
3.1 Design of the study 11
3.2 Cleaning process 12
3.3 Optimization of paste of photoanode 12
3.4 Optimization of blocking/compact layer 14
3.5 Electrolyte for optimization groups 14
3.6 Counter electrodes for optimization groups 15
3.7 Dye for optimization groups 15
3.8 Compact layer 15
3.9 Blocking layer 15
3.10 Preparation of paste of photoanode 15
3.11 Design of multilayers 16
3.12 Preparation of electrolyte 17
3.13 Preparation of counter electrode 17
3.14 Dye loading process 18
3.15 Fabrication of the DSSCs 18

CHAPTER 4 DEPOSITION AND CHARACTERIZATION METHODS 19
4.1 Spin coating 19
4.2 XRD measurements 20
4.3 UV-VIS-NIR spectroscopy measurements 21
4.4 Atomic force microscopy measurements 21
4.5 Thickness measurements 22
4.6 Quantum efficiency measurements 23
4.7 Current- voltage measurements 25
CHAPTER 5 RESULTS AND DISCUSSION 27
5.1 XRD results 27
5.2 Optical profilometer results 28
5.3 Atomic force microscopy results 29
5.4 EQE results 31
5.5 UV-VIS-NIR results 32
5.6 Results of current-voltage measurements 36
5.7 Discussion of results 38
REFERENCES……..40
CURRICULUM VITAE……...45

ABBREVATIONS

AFM	Atomic force microscopy
CdSe	Cadmium selenide
CdTe	Cadmium telluride
CIS	Copper-indium-gallium-selenide
DSSC	Dye-sensitized solar cell
EtOH	Ethanol
FTO	Fluorine-doped tin oxide
GaAs	Gallium arsenide
I^-	Iodide
I_3^-	Triiodide
InP	Indium phosphide
ITO	Indium-tin oxide
LiI	Lityum İyodur
Nb_2O_5	Niobium pentoxide
Pt	Platinum
PV	Photovoltaic
Red-Ox	Reduction /Oxidation
RPM	Revolution per minute
Si	Silicon
SnO_2	Tin dioxide
TCO	Transparent conductive oxide
TiO_2	Titanium dioxide
TTIP	Titanium (IV) isopropoxide
UV-VIS-NIR	Ultraviolet-visible-near infrared
XRD	X-ray diffraction
WO_3	Tungsten trioxide
ZnO	Zinc oxide

LIST OF SYMBOLS

J_{sc}	Short circuit current density
V_{oc}	Open circuit voltage
FF	Fill factor
η	Efficiency
I_{mp}	Current at the maximum power point
I_{sc}	Short-circuit current
V_{mp}	Voltage at the maximum power point
P_{in}	Power of the incident light
D	Sensitizer dye
D^*	Excited energy state of the sensitizer dye
D^+	Oxidized state of the sensitizer dye
R_s	Series resistance
R_{sh}	Shunt resistance
M	Molarite
λ	X-ray wavelength
d	Distance between planes in the atomic lattice
2θ	Diffraction angle

LIST OF TABLES

Table 3.1 Design of multilayer-based photoanode structure..... 17
Table 5.1 Grain size and anatase weight percentage values for the samples 28
Table 5.2 AFM results for the samples 29
Table 5.3 External parameters of the investigated DSSCs..... 38

LIST OF FIGURES

Figure 2.1 Basic structure of DSSCs [9, 10] 3
Figure 2.2 DSSC's basic kinetic process and energy diagram [18] 6
Figure 2.3 Equivalent circuit model of DSSC [19] 7
Figure 2.4 Light responses of the objects [20] 8
Figure 2.5 Recombination types for charge carriers [22] 9
Figure 3.1 Structure of multilayer DSSCs 11
Figure 3.2 Cleaning of FTO coated glass substrates 12
Figure 3.3 Optimization of paste 13
Figure 3.4. External parameters of the cells made of different pastes 13
Figure 3.5. Determination of the optimum thickness of blocking layer 14
Figure 3.6 The structure of the samples 16
Figure 3.7. Investigated samples before and after dye loading 18
Figure 4.1 Spin coating technique application [36] 19
Figure 4.2 Rigaku Miniflex 600 XRD [38] 20
Figure 4.3 UV-VIS-NIR spectrophotometer [39] 21
Figure 4.4 AFM working principle [41] 22
Figure 4.5 Quesant Ambious Q-scope series AFM 22
Figure 4.6 Optical profilometer working principles [43] 23
Figure 4.7 Optical profilometer working principles [44] 23
Figure 4.8 Equipment for external quantum efficiency measurements [46] 24
Figure 4.9 Quantum efficiency measurement system [47] 24
Figure 4.10 Current-voltage curve for solar cells [48] 25
Figure 5.1 XRD patterns of the samples 27
Figure 5.2 2D and 3D topographical AFM pictures of samples. 30
Figure 5.3 External quantum efficiency of the investigated DSSCs 31
Figure 5.4 Layer-by-layer improvement of EQE 32
Figure 5.5 Absorbance spectrum of the samples before and after dye loading 34
Figure 5.6 Absorbance spectrum of the all samples 34
Figure 5.7 Layer-by-layer and cumulative enhancement of absorbance before dye 35
Figure 5.8 J-V results for the samples 37
Figure 5.9 Change in external performance parameters 37

Guide on how to read the thesis

This M. Sc. Thesis consists of five chapters.

Chapter 1 consists of the introduction and provides basic information about solar cells.

Chapter 2 covers specific information about solar cell types in terms of charge mechanisms.

Chapter 3 includes the study's experimental process, and how the DSSCs were designed, including how their multiple layers were applied.

Chapter 4 discusses the methodologies utilized for the fabrication and characterization processes.

Chapter 5 presents the results and discussion.

CHAPTER 1

INTRODUCTION

The demand for energy is steadily increasing. Fossil fuels are exhaustible sources and pollute the environment. Therefore, people need to use alternative renewable energy sources [1]. Solar, wind, geothermal, hydroelectric, and biomass are well-known renewable energy sources. Among others, solar energy is a significant and promising source in terms of many aspects, such as easy transportation and free availability.

Photovoltaic devices convert the energy of incident light coming from the sun into an electrical current, which is based on the photoelectric effect. The term photovoltaic is a combination of *light* and the surname of Alessandro *Volta,* inventor of the electrical battery [2]. The photoelectric effect is related to the absorption of electromagnetic radiation, which excites charged particles, namely electrons, from the surface of the material [3]. Einstein discovered the photoelectric effect in 1905, and he received the Nobel Prize in 1921 for discovery [4].

When considering the working principle of solar cells, they can be classified as either conventional or excitonic solar cells. Excitonic solar cells are also divided into two main groups which are known as dye-sensitized solar cells (DSSCs) and organic solar cells (OSCs).

In 1991, M. Grätzel et *al*. introduced DSSCs. They designed the first DSSC, the "Grätzel cell"; which converted solar energy chemically into electrical energy by using mesoporous TiO_2. This was a breakthrough in the field, leading DSSCs to become popular among researchers. Since DSSCs are environmentally friendly and can be fabricated at a low-cost, they are considered promising alternatives to silicon-based solar cells [5].

Wide-bandgap semiconductor materials, such as TiO_2, are mostly preferred for DSSCs. TiO_2 can only absorb ultraviolet light (smaller than 387 nm in wavelength).

Dye molecules are adsorbed on the TiO_2 layer, providing absorption of visible light, this resulting in more efficient absorption of the sunlight's spectrum.

Traditional solar cells are based on *p-n* junction solar cells. Fundamentally, they consist of three layers which are a *p-type* layer, an *n-type* layer and metal contacts. When the light reaches the absorber layer, an electron excites into a higher energy level from a lower energy level. A potential voltage difference occurs between the layers. Due to the electrical field formed at the junction, electrons and holes are separated from each other, and they transport through a length to reach metal contacts. In order to prevent random motion of the free electrons and to create a directed current flow, the nature of the junction is important for *p-n* junction solar cells. Si, GaAs, and InP are widely used materials for this type of solar cells.

Contrary to *p-n* junction solar cells, light absorption and charge separation processes occur at different parts of DSSCs. Dye is responsible for light absorption and sensitization, while the semiconductor (TiO_2) plays a role in charge transport [6]. In excitonic solar cells, excitons are generated by light absorption and separated immediately at interfaces of each layer of the cell. Photo-generated charge carriers are diffused throughout DSSCs. While high-quality structural features are required for *p-n* junctions due to defects behaving as recombination centers in the bulk structure, this phenomena can be compensated for in excitonic solar cells due to their districted functionalized layers. Therefore, fabrication costs are reduced. The theoretical maximum achievable photovoltaic conversion efficiency known as the Shockley-Queisser limit of DSSCs, is similar to that of traditional cells [7, 8].

CHAPTER 2

DYE-SENSITIZED SOLAR CELLS

DSSCs are classified as excitonic solar cells. Their working principle resembles the photosynthesis loop that occurs in nature.

2.1 Components

DSSCs consist of four major components, which are the photoanode, photosensitizer, electrolyte, and counter electrode, as represented in Fig 2.1.

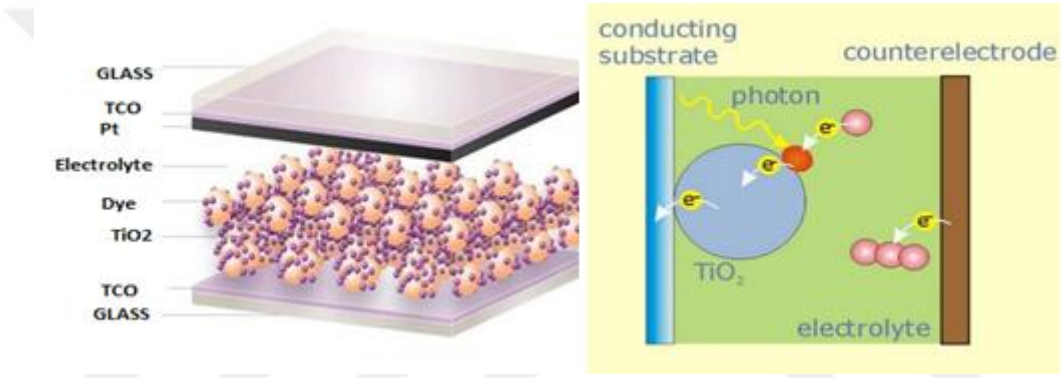


Figure 2.1 Basic structure of DSSCs [9, 10]

The photoanode can be considered as the base for the DSSCs due to it being an electron transport framework. It consists of a transparent conductive oxide (TCO) coated on a glass substrate. TCOs are generally used for optoelectronic applications [11]. Flourine-doped tin oxides (SnO_2:F, FTO) and indium-doped tin oxides (SnO_2:In, ITO) are widely employed as TCOs in solar cells. However, FTO is more stable for the annealing process at 500˚C. In addition to this, it has an advantage over ITO due to its superior optical properties in the visible region [12].

Photoanodes are made by coating wide-band gap metal oxides (TiO_2, ZnO, SnO_2, Nb_2O_5, CdSe, CdTe) onto TCOs [13]. In this work, FTO-coated glass substrates were preferred for providing electrical contacts for the TiO_2-coated photoanode and counter electrodes of the solar cell.

TiO_2 is frequently used as a photoanode material because of its wide band gap energy (3.2eV) value, easy production features, non-toxicity and low cost. TiO_2's large band gap energy provides it with the ability to absorb wavelengths smaller than 387 nm in UV region of the incident light spectrum [14]. Loading dye molecules onto TiO_2 makes absorption of visible light possible.

TiO_2 has three known phases: anatase, rutile, and brookite. The anatase phase is generally used for DSSCs, since it exhibits high mobility [13]. However, commercialized powder such as Degussa P25 powder, includes 80 % anatase and 20 % rutile phases of TiO_2. G. Li et *al.* studied on the synergetic effects of the combination of anatase and rutile phases and concluded that up to 13 wt % rutile improved short circuit current results [15].

The porous structure of the photoanode is an important factor for dye adsorption and the related absorbance performance. A TiO_2-based *n-type* semiconductor layer should be a porous structure. The size of the pores defines the porosity level: Materials are can be microporous, mesoporous and macroporous, with porosity of lower than 2 nm, between 2 to 50 nm, and larger than 50 nm, respectively. Generally, a mesoporous structure for TiO_2 is preferred for DSSCs. Although, porosity is highly desired, there is a trade-off of between high dye adsorption ability and electrical path connectivity. In other words, increasing pores can give rise to more dye adsorption and absorbance of light. However, macropores can cause the TiO_2 framework to collapse or cut off electron flow due to connection loss.

Particle size is a determining factor when defining the pore size of a structure. Generally, nanopowders are used to obtain a high active surface area, and mesoporous structures are constructed to increase optical performance.

According to the literature, the ideal photoanodes have the following features:

- High surface area to improve dye absorption
- Supply fast electron transfer from dye to outer circuit
- Porous structure for diffusion of dye and electrolyte
- Suitable material in terms of resistance to photo-corrosion

- Behave as a good electron acceptor
- Supply optimum interface between contact with dye and the conductive layer. [16]

In addition to the fundamental photoanode layer, compact blocking layers can also be used between the main absorbance TiO_2 layer and FTO to inhibit current leakage and undesired recombination between interfaces. By the way, the thickness of the blocking layer is important, and it should be determined properly. If the thickness is greater than the diffusion path of the charge carriers, electrons start to recombine before arriving at collection points, and this give rise to a decrease in short circuit current and efficiency values. On the other hand, a significantly thin blocking layer also cannot sufficiently block current leakage. Therefore, there is a trade-off between blocking layer thickness and solar cell short circuit current value [16].

Dye molecules are crucial components of DSSCs. They are attached to the surface of the mesoporous TiO_2 layer to help absorb the visible light spectrum. Many different types of dyes can be used to sensitize the layer, such as natural, organic or metal-complex dyes. According to the literature, ruthenium and osmium polypyridine metal complex are promising candidates due to their high absorption ability and long excited-state lifetime features. However, they are high in price [13, 17].

Depending on the included chemical compounds, there are many candidates to absorbing visible light from natural sources. Dye extractions from fruits, vegetables, flowers or leaves can be used as alternative, cost-effective sensitizers.

The electrolyte is another core component which is responsible for regeneration of excited dye molecules. A good electrolyte candidate for DSSCs should provide high conductivity, low viscosity, proper contact behavior, and should not absorb the visible light spectrum.

Mostly liquid electrolytes are used as a charge transport medium for DSSCs. A liquid electrolyte contains basically a redox couple and a solvent. I^-/I_3^-, Br^-/Br_3^-, and Co^-/Co_3^- are the primary alternatives for redox couples. But I^-/I_3^- is preferred in the literature.

The counter electrode is responsible for transporting electrons from the external circuit into the electrolyte. Platinum is preferred due to its superior catalytic activity and connectivity. It is the pioneering catalyst to facilitate reduction activity [13]. However, it is a rare element and relatively expensive. Therefore, scientists are searching for new alternatives for counter electrodes and have investigated other catalysts, such as carbon, graphene or polymers.

2.2 Working principles

When sunlight impinges on the dye molecules adsorbed by TiO_2, the electrons of the dye molecules are excited to the conduction band of TiO_2. The dye molecules each lose an electron. Next, the photo-generated electrons are diffused through mesoporous TiO_2 photoanode to the contacts. Electrical current is provided at an external circuit path as shown in Fig. 2.2. Oxidized dye molecules are regenerated by the redox electrolyte. Electrons which arrived at the cathode can easily pass into the solar cell structure thanks to high conductivity and the catalytic activity of the counter electrode.

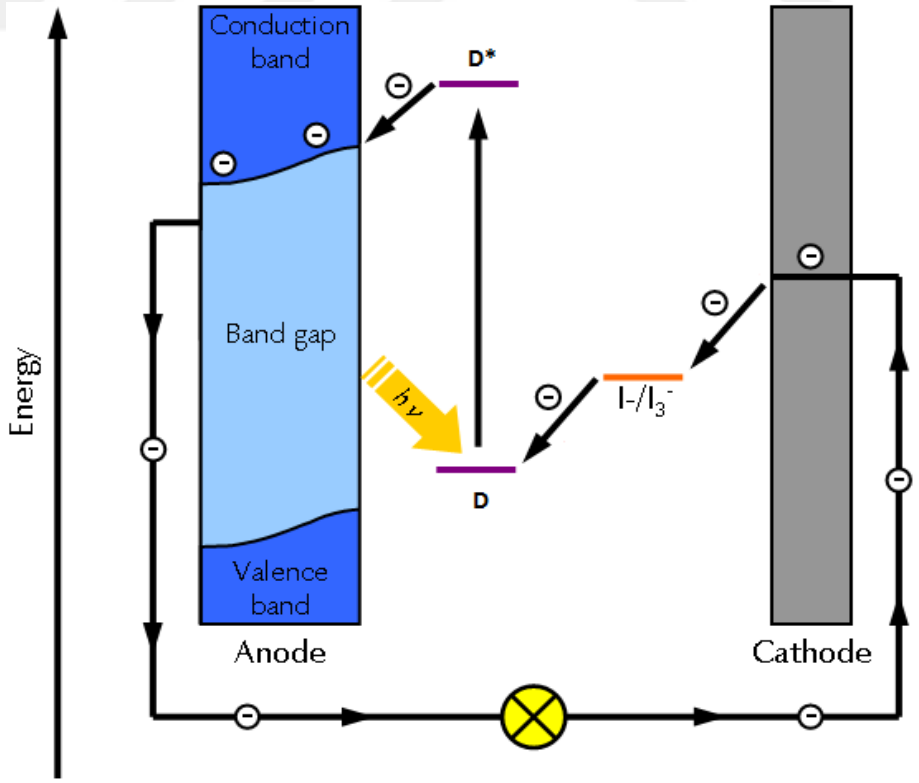


Figure 2.2 DSSC's basic kinetic process and energy diagram [18]

Kinetic processes in DSSCs can be expressed with the following formulas:

$D + h\nu \rightarrow D^*$	photo-excitation	(2. 1)
$D^* \rightarrow e^-(in\ TiO_2) + D^+$	charge injection	(2. 2)
$D^+ + 3I^- \rightarrow D + I_3^-$	regeneration	(2. 3)
$D^+ + e^- \rightarrow D$	recombination	(2. 4)
$I_3^- + 2e^- \rightarrow 3I^-$	back reaction	(2. 5)

Equation (2.1) refers to the light absorption process. Excited dye molecules give up an electron to TiO_2 in Eq. (2.2). Oxidized dye molecules are regenerated by the redox electrolyte in Eq. (2.3),and by absorbing an electron in Eq. (2.4). Eq. (2.5) describes the regeneration of the I^- molecules at during reaction.

2.3 Equivalent circuit

DSSCs are typically modeled by a diode as in Fig. 2.3. Illumination is indicated by a current source and losses are shown with serial (R_s) and shunt (R_{sh}) resistances.

The source of R_s covers contact resistances, and reverse currents. R_s directly influences fill factor (FF) value. High values of R_s lower the short circuit current (I_{sc}) drastically, but slightly affect the open-circuit voltage (V_{oc}). R_s should be minimized to overcome losses.

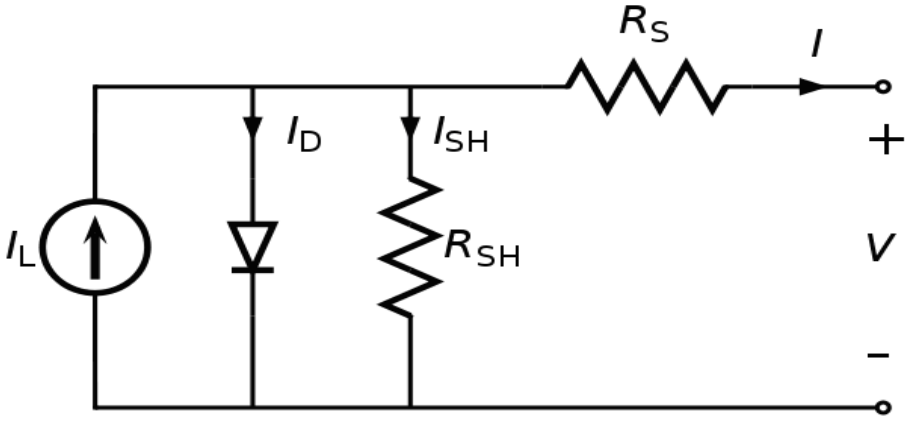


Figure 2.3 Equivalent circuit model of DSSC [19]

R_{sh} is related to defects in the material and its porous structure. An electrical current can find alternative, undesired low-resistive paths due to the presence of defects. This causes a significant drop in V_{oc}, and also influences I_{sc} and FF values. High shunt resistance is expected as an indicator of high-quality films.

2.4 Losses

The materials are transparent to, absorptive of, or reflective of the incoming light depending on different wavelengths and the band gap of the material, as shown in Fig. 2.4. If the incoming light energy is greater than the band gap energy of the material, it absorbs light and excites an electron. For DSSCs, the goal is to absorb as much light as possible and generate more excitons. If the material is transparent to or reflective of light at a certain wavelength, light passes directly through the material, and it becomes useless as a solar cell. Non-absorption of photons is a kind of optical loss.

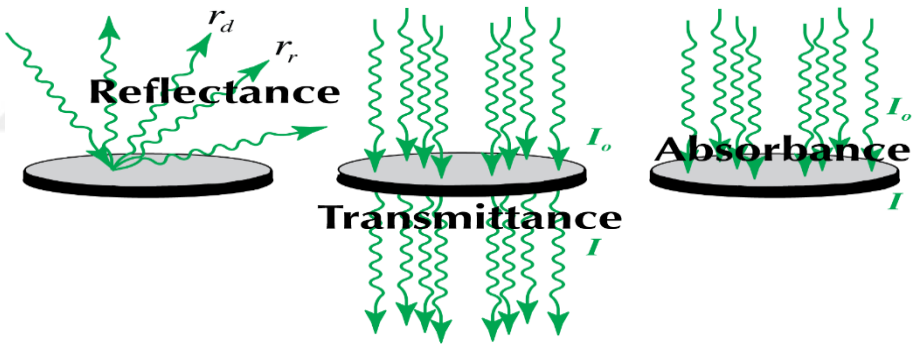


Figure 2.4 Light responses of the objects [20]

Another loss mechanism is the recombination of charge carriers. It is a term which depicts the combination of generated electron-hole pairs in equilibrium before contributing to the current [21]. Recombination can be categorized as radiative, Shockley-Reed-Hall, or Auger as shown in Fig. 2.5. Radiative (band to band) recombination arises from the direct loss of charge carriers causing radiation. Generally, it occurs at direct band gap materials. Shockley-Reed-Hall recombination took its name from those that discovered it and is related to defects mediated on semiconductor and extra mid-gaps. The last recombination is the Auger recombination. If a hole is refilled with an electron from a higher energy level

without emitting radiation energy, then it generates a new electron-hole pair which is called an Auger electron [22, 23].

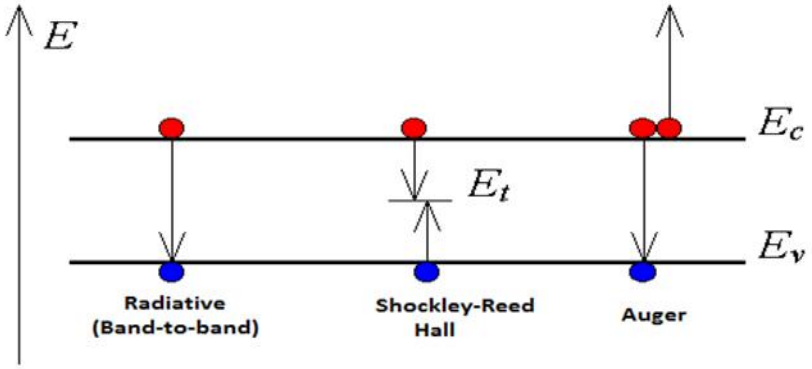


Figure 2.5 Recombination types for charge carriers [22]

2.5 Literature Review

Sedghi et. *al.* prepared a TiO_2 paste with different solvents (acetylacetone, ethanol, acetylacetone and ethylene) [24]. The paste which was prepared by utilizing acetylacetone showed fewer cracks and the results were relatively better, with an efficiency of 3.8 %. By applying a $TiCl_4$ treatment, efficiency was enhanced from 3.9 % to 5.1 % due to suppression of recombination.

Park et *al.* observed a positive effect on cell performance, when applying a different thickness of $TiCl_4$ treatment due to increasing electron lifetime [25]. Efficiency was boosted from 8.12 % to 9.48 %.

Lee et *al.* studied DSSCs with different particle sizes for the multilayer structure and pointed out the higher efficiency of the state in which the largest particle size paste was positioned at top level. This was due to the paste behaving as a light scattering layer [6]. They reported an efficiency value of 5.24 %.

Yang et *al.* revealed the effect of hierarchical TiO_2/ZnO blocking layers (BL) on current and efficiency results. [26] TiO_2 BL alone provides an enhancement to the current, and ZnO produce the opposite effect due to interactions between ZnO BL and the acidic dye used for insulation. The V_{oc} value increased when only ZnO BL was used. By coating TiO_2 BL onto ZnO BL; the ZnO-dye reactions were inhibited and this resulted in a significant increase in efficiency.

Jeng et *al.* correlated the particle size and expected thickness of the TiO_2 layer to get maximum efficiency [27]. The results indicated that using large particles-thinner films (about 6 μm) on smaller particles (21 nm)-thicker films (12 μm) gives better results in terms of efficiency.

Yu et *al.* immersed the mesoporous TiO_2 film into an organic titanium solution prepared from tetrabutyl titanate. Therefore, the FTO/ TiO_2 interface and connectivity is improved [28]. Due to low viscosity, the porosity ratio did not change significantly to maintain dye adsorption conditions, as it was assumed. Efficiency results were 5.71 % and 7.32 % for bare and sol-modified sample, respectively.

Pan et *al.* considered enhancement of the TiO_2 electron pathway with a recipe of modified P25+ TiO_2 anatase powder which favored photoelectrical properties [29].

Kontos et *al.* mixed the commercial P25 TiO_2 powder with titania sol-gel and empowered the bonds between titanium molecules [30]. However, this induced roughness and porosity, and doubled the current results by preventing short-circuiting of the liquid electrolyte in the TiO_2 network. They also reported that increasing the nano-sized TiO_2 particles enabled more absorption of light.

Kadachi et *al.* applied TiO_2 paste with the doctor blade method onto a spin-coated blocking layer [31]. They compared natural mallow dye and Ruthenium-based N3 dye. They claimed that mallow dye gives promising results in terms of efficiency.

Wang et *al.* reported that Eosin Y dye, and Br^-/Br_3^- provided better results [32]. The Eosin Y dye and Br redox couple doubled efficiency compared to the iodine redox couple. On the other hand, N719 iodine performed almost 5 times better in terms of short circuit current and efficiency values. This study emphasized the importance of the selection criteria for the dye and electrolyte combination.

Chien et *al.* studied various Ethyl cellulose (EC) percentages (2-18 wt %) of TiO_2 paste. 10 wt % was the best with 7.53 % of efficiency [33]. They claimed a small addition of EC was insufficient while, an excessive addition of over 10 wt % causes extra-large pores and obstructs the carrier transport.

CHAPTER 3

EXPERIMENTAL WORK

3.1 Design of the study

As a starting point, TiO_2 paste was optimized to be crack-free, and have good adherence on the FTO surface [34]. We followed the methodology reported by Ito et *al*. [34]

One of our designs with multilayers is shown in Fig. 3.1. Different compact TiO_2 layers from different precursors with post-treated extra connection layers were proposed. The effect of the thickness of the mesoporous TiO_2 layer was also investigated.

Optimization experiments were done to assess the thickness of the spin-coated TiO_2 blocking layer. When considering the optimum thickness of the blocking layer, various multilayer structures were examined.

For optimization experiments, relatively cheaper dye (Eosin B), a simple redox electrolyte solution and cost- effective counter electrode chemicals were utilized. After that, real experiments were repeated with more promising chemical compounds reported in the literature.

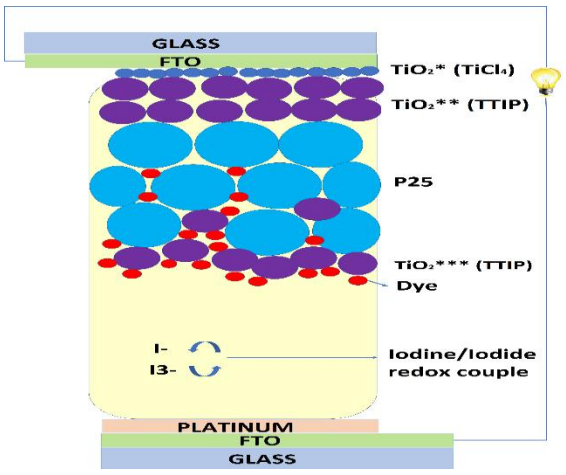


Figure 3.1 Structure of multilayer DSSCs

After the construction of multilayer-based photoanodes, the samples were characterized before dye loading, as will be explained in Chapter 4. Before dye loading, structural, morphological, and optical characterizations were obtained without destroying films.

3.2 Cleaning process

FTO coated glasses were firstly washed with detergent then rinsed with tap water, as in Fig. 3.2. Next, an ultrasonic cleaning process was realized by using deionized water, ethanol, then deionized water again for 5, 10 and 5 minutes, respectively. Cleaned samples were dried at 80˚C in ambient air.



Figure 3.2 Cleaning of FTO coated glass substrates

3.3 Optimization of photoanode paste

P25 TiO_2 powder (Evonik, Degussa, 21 nm), ethyl cellulose (EC) (Sigma Aldrich, 46070, 7-15 mPa.s), ethyl cellulose (Sigma Aldrich, 46080, 30-70 mPa.s), and terpineol (Sigma Aldrich, 86480) were used to prepare a homogenous paste following the method of Ito et *al.* [34]. Viscosity values were different for two types of EC. Terpineol, EC and P25 were used as a dispersant, thickener and precursor source, respectively. All chemicals had the proper degree of purity. The mixing of these ingredients was carried out in a baker. Since cracks between FTO and TiO_2 can destroy electron transport, main goal was to obtain a crack-free, homogenous, viscous paste.

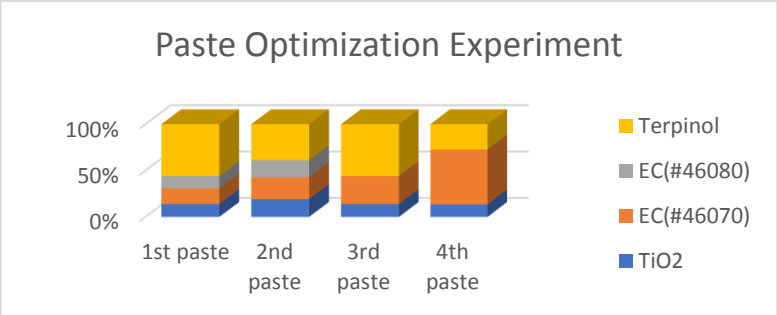


Figure 3.3 Optimization of paste

EC and terpinol ratios were systematically changed to control the properties of the paste as in Fig. 3.3. In the first paste formula, the amount of terpineol was doubled. In the 2nd paste, viscous EC was doubled. In the 3rd paste, low-viscosity EC was utilized only and finally, in the 4th paste low-viscosity EC was doubled. According to the J-V results as shown in Fig. 3.4, and by considering relatively high external performance parameters, the 1st paste was chosen for further experiments.

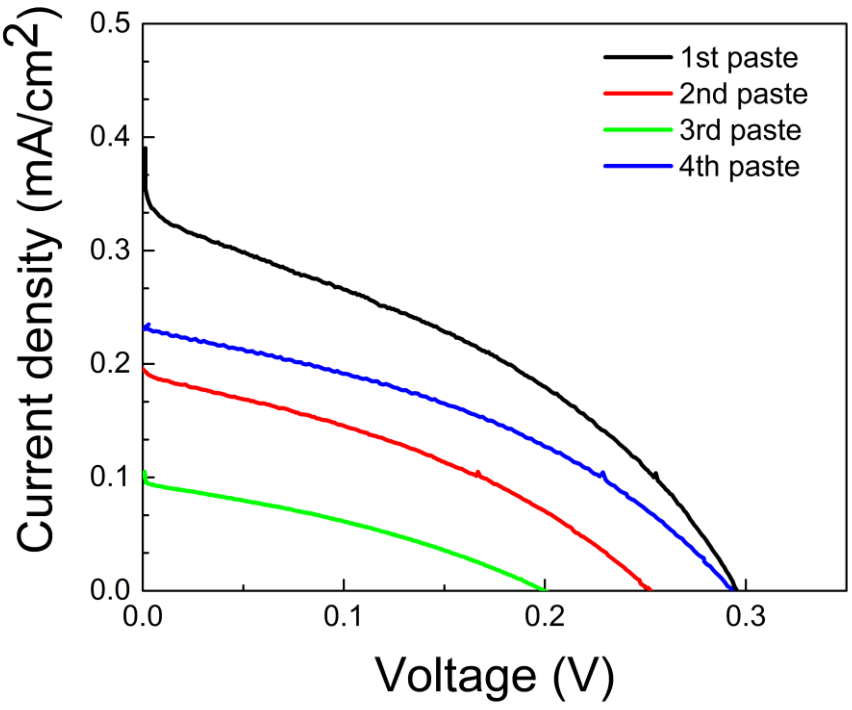


Figure 3.4. External parameters of the cells made of different pastes

3.4 Optimization of blocking/compact layer

0.6 M sol was prepared by using Titanium (IV) isopropoxide (TTIP, Sigma Aldrich, 205273), acetic acid (Sigma Aldrich, 27225), and triethylamine (Sigma Aldrich, T0886). They were separately dissolved in ethanol (Merck, 100983) for 15 min at 400 rpm. They were mixed together for 2h at 400 rpm, and 50˚C, and the prepared sol was then aged for 21 h at room temperature. TiO_2 layers with varying thickness were coated on cleaned FTO substrates using a spin coater (2000 rpm, 0 rpm/s, 30 s) to examine the effect of the thickness of the blocking layer on efficiency while all other parameters were kept constant. 1, 2, 3, and 5 coating cycles were examined. By applying of sol to the film and pre-heating at 500˚C for 5 min, one coating cycle was obtained. Given the results shown in Fig. 3.5, a blocking layer with 5 coating cycles was selected for further studies.

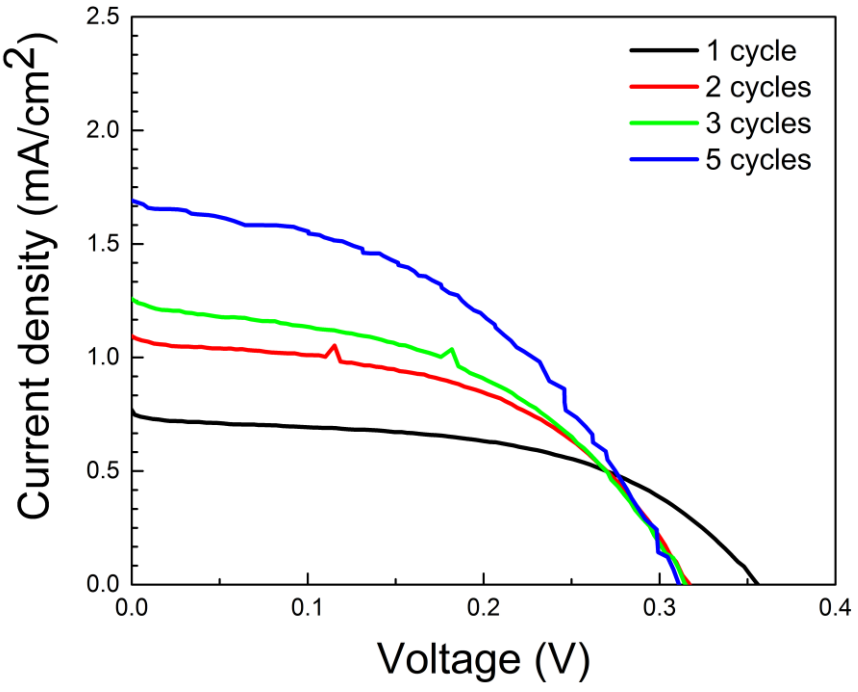


Figure 3.5. Determination of the optimum thickness of blocking layer

3.5 Electrolyte for optimization groups

The iodine/triiodide electrolyte solution included 0.05 M Iodine (I_2, Sigma Aldrich, 207772), 0.5 M Lithium iodide (LI, Merck, 818287) and acetonitrile (Sigma Aldrich,

34851). I_2 and LI were dissolved separately and mixed in an acetonitrile solvent using a magnetic stirrer for 2 hours.

3.6 Counter electrodes for optimization groups

Platisol (T/SP, Solaronix, 41222) was applied via spin coating method onto cleaned FTO for 20 layers, and then it was annealed at 450˚C for 30 minutes.

3.7 Dye for optimization groups

Eosin B (Alfa, A17377) synthetic dye was used as a sensitizer. Samples were immersed in 0.03 mM Eosin B dye-ethanol solution for 3 h at 50˚C for dye loading.

3.8 Compact layer

A 2 M aqueous Titanium (IV) chloride ($TiCl_4$,Sigma Aldrich, 280566)- deionized water (DI) stock solution was prepared at approximately 0˚C to eliminate violent reaction. 40 mM of the $TiCl_4$ solution was diluted from the stock solution of 2 M. Regardless of control sample, all samples were dipped into $TiCl_4$ at 75˚C for 30 minutes. According to Choi et *al.* 25 nm of thickness was expected with this recipe [35]. To reduce stress, samples were also annealed at 500˚C for 30 minutes.

3.9 Blocking layer

When considering, the optimum thickness of the blocking layer, a TTIP solution was prepared and deposited as 5 layers with a spin coater. 15µl of TTIP sol was deposited at 500˚C for 5 min pre-heating and annealed at 500˚C for 1h.

3.10 Preparation of photoanode paste

4.24g of P25 nano-powder and 9.28g EC stock solution were dissolved in 18.4ml terpinol to obtain the paste. EC stock solution covered two different powders having different viscosities (7-15mPa and 30-70mPa) with 56.25 wt % and 43.75 wt % as mentioned previously. Spin coating was carried out in two steps to adjust the uniformity (2000 rpm, 30s and 3000 rpm, 30s) of the films. Samples were pre-heated at 500˚C for 15 min.

The TTIP solution was coated onto the P25 paste using a spin coater with 3 drop cycles (2000 rpm for 30s) and 1 pre-heating cycle (500 ˚C for 5min).

To understand the effect of the absorption layer thickness, the P25 paste and TTIP solution were applied again.

3.11 Design of multilayers

Following Table 3.1, five samples were prepared as shown in Fig. 3.6. Hereafter, the samples will be called N1, N2, N3, N4, and N5. First, P25 viscous paste was applied onto bare cleaned FTO (see N1). To recognize the effect of the compact titanium layer, $TiCl_4$ treatment was applied onto FTO by dipping into a 40 mM $TiCl_4$- DI solution (see N2). In the third sample (N3), TTIP solution was coated with a spin coater to observe the effect of the TiO_2 blocking layer. To improve morphological features, TTIP solution was applied onto the viscous P25 paste in the the fourth sample (N4). TTIP solution provided smaller particles and more homogenous dissemination. Finally, the effect of the doubled P25 layer was examined in the fifth sample (N5).

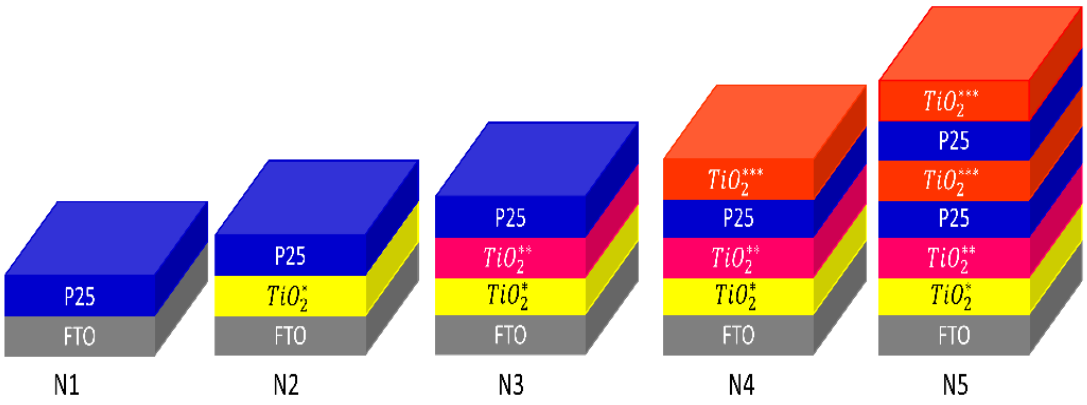


Figure 3.6 The structure of the samples

Table 3.1 Design of multilayer-based photoanode structure

Repeat cycle	Process explanation	Sample N#				
		N1	N2	N3	N4	N5
1	FTO cleaning					
1	$TiCl_4$ treatment at 75˚C for 30 min					
1	Annealing at 500˚C for 30 min					
5	TTIP sol deposition (2000 rpm, 30 s)					
5	Pre-heating at 500˚C for 5 min					
1	Annealing at 500˚C for 1h					
1	P25 paste deposition (2000 rpm, 30 s, 3000 rpm, 30 s)					
1	Pre-heating at 500˚C 15 min					
3	TTIP sol deposition (2000 rpm, 30 s)					
1	Pre-heating at 500˚C for 5 min					
1	P25 paste deposition (2000 rpm, 30 s, 3000 rpm, 30 s)					
1	Pre-heating at 500˚C for 15 min					
3	TTIP sol deposition (2000 rpm, 30 s)					
1	Pre-heating at 500˚C for 5 min					
1	Annealing at 500˚C for 1h					

3.12 Preparation of electrolyte

0.6 M of 1-Butyl-3-methylimidazolium iodide (BMII, Sigma Aldrich, 713066), 0.5M 4-tert-Butylpyridine (TBP, Sigma Aldrich, 142379), 0.1M LiI (Merck, 818287), 0.05 M I_2 (Sigma Aldrich, 207772) and acetonitrile (Sigma Aldrich, 34851) were mixed with hot stirrer at 400 rpm for 2 h.

3.13 Preparation of counter electrode

Chloroplatinic acid hydrate ($H_2PtCl_6.xH_2O$, Sigma Aldrich, 520896, trace metals basis), and 2-propanol (Sigma Aldrich, 278475) were used. 5mM $H_2PtCl_6.xH_2O$ was dissolved in 2-propanol solvent. 20 coating cycles were applied on FTO glass with spin coater (2000 rpm, 5rpm/s, 30s). Counter electrodes were annealed at 450˚C for 30 minutes for activation.

3.14 Dye loading process

Di-tetrabutylammonium cis-bis(isothiocyanato) bis(2,2′-bipyridyl-4,4′-dicarboxylato) ruthenium(II) (Sigma Aldrich, 703214) known as N719 in the literature was used to sensitize the samples. A 0.3 mM of N719 -Methanol (Sigma Aldrich, 67-56-1) solution was prepared and protected from heat and light. The dye immersion process took 18 h, 45 min.

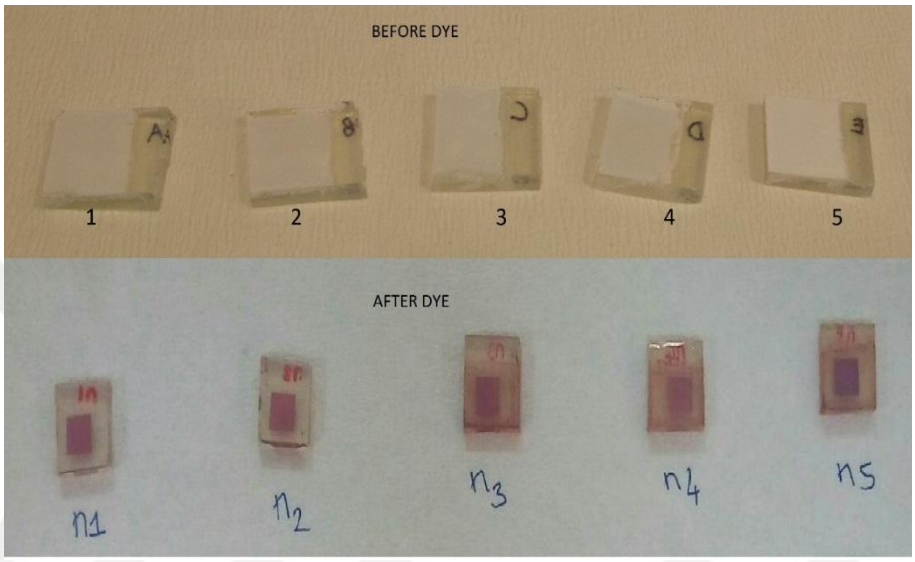


Figure 3.7. Investigated samples before and after dye loading

3.15 Fabrication of the DSSCs

All components were combined in a sandwich structure. The electrolyte was dropped into working and counter electrodes. From contacts, I-V measurements were carried out with crocodile cables under 0.3 sun intensity test conditions using a solar simulator.

CHAPTER 4

DEPOSITION AND CHARACTERIZATION METHODS

In the deposition process for the photoanodes, a spin coater was used. Structural, morphological and optical properties of the coated photoanodes were determined by means of X-ray Diffractometer, Atomic Force Microscope and UV-VIS-NIR Spectrophotometer, respectively. Using a combination of the dye loaded photoanode and Platinum-coated counter electrode, solar cells were fabricated. Finally, performance of the solar cells was investigated by means of external quantum efficiency and current - voltage measurements.

4.1 Spin coating

The spin coating technique illustrated in Fig. 4.1 is a low-cost deposition process, which aims to realize a uniform deposition. Generally, when the target chemical is dissolved in a proper solution, it spreads out uniformly onto the desired substrate due to centripetal force. The deposition process has some parameters, such as revolution per minute (rpm) speed, rotary time, and acceleration speed to control thickness. During rotation, as the liquid solvent moves away, dried and stabilized surfaces are obtained.

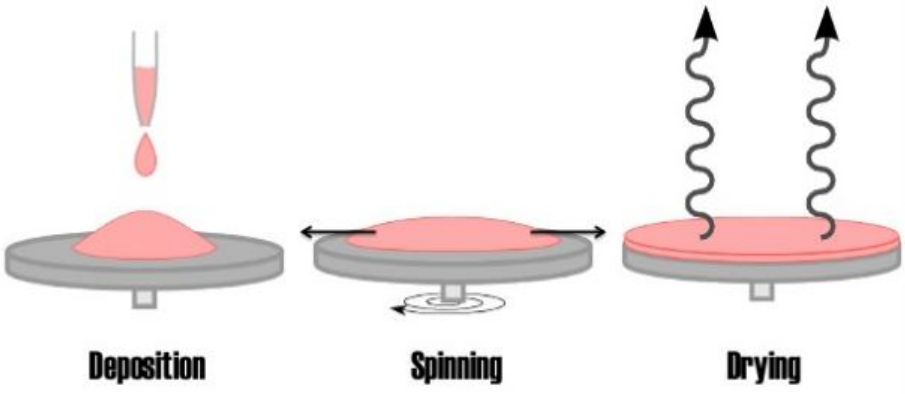


Figure 4.1 Spin coating technique application [36]

4.2 XRD measurements

XRD measurements are employed to characterize the structural properties of materials using the Bragg equation. In the formula shown in Eq. 4.1. λ the characteristic wavelength (0.1542 nm) of the X-rays impinging on the sample, d is the interplanar spacing between aligned atoms, and θ is the angle of the X-ray beam with planars [37].

$$n\lambda = 2dsin\theta \tag{4.1}$$

In this study, the crystal structure of the photoanodes was investigated by a Rigaku Miniflex 600 Table Top Powder X-ray diffractometer (Fig 4.2) using Cu anode material operating at 40 kV and 15 mA. The diffraction patterns were collected over 20-60 ° with a step size of 0.02 °. Results were analyzed using PDXL software.



Figure 4.2 Rigaku Miniflex 600 XRD [38]

4.3 UV-VIS-NIR spectroscopy measurements

The UV-VIS-NIR spectroscopy measurement system includes a light source and detector mechanism to detect how much light passes through or has been absorbed, as shown in Fig. 4.3. In this study, a Schimadzu UV-VIS-NIR 3600 Spectrophotometer was utilized for the investigating samples before and after dye immersion to determine the optical contribution of the dye molecules.



Figure 4.3 UV-VIS-NIR spectrophotometer [39]

4.4 Atomic force microscopy measurements

Atomic force microscopy (AFM) is a tool used to examine the surface morphology of materials. AFM contains a tip on edge of a cantilever which has piezoelectric properties. According to the tip position, AFM works in two modes; contact and non-contact. Contact mode can damage the surface of the sample. In non-contact mode, once when tip becomes close enough to the surface, AFM starts to oscillate at resonance frequency and scan the sample in x-y directions as in Fig. 4.4. The incoming laser angle changes due to surface properties. This is detected by photodetector and analyzed using software [40]. In this study, the Quesant Ambious Q- scope series AFM shown in Fig 4.5, was used to measure a 5x5 μm^2 area of the samples.

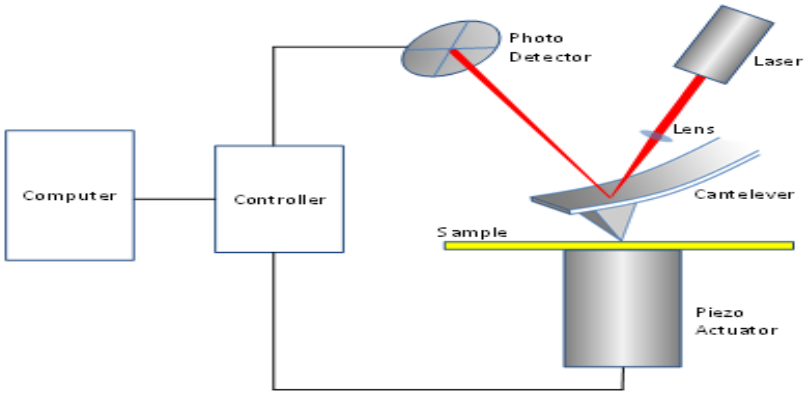


Figure 4.4 AFM working principle [41]

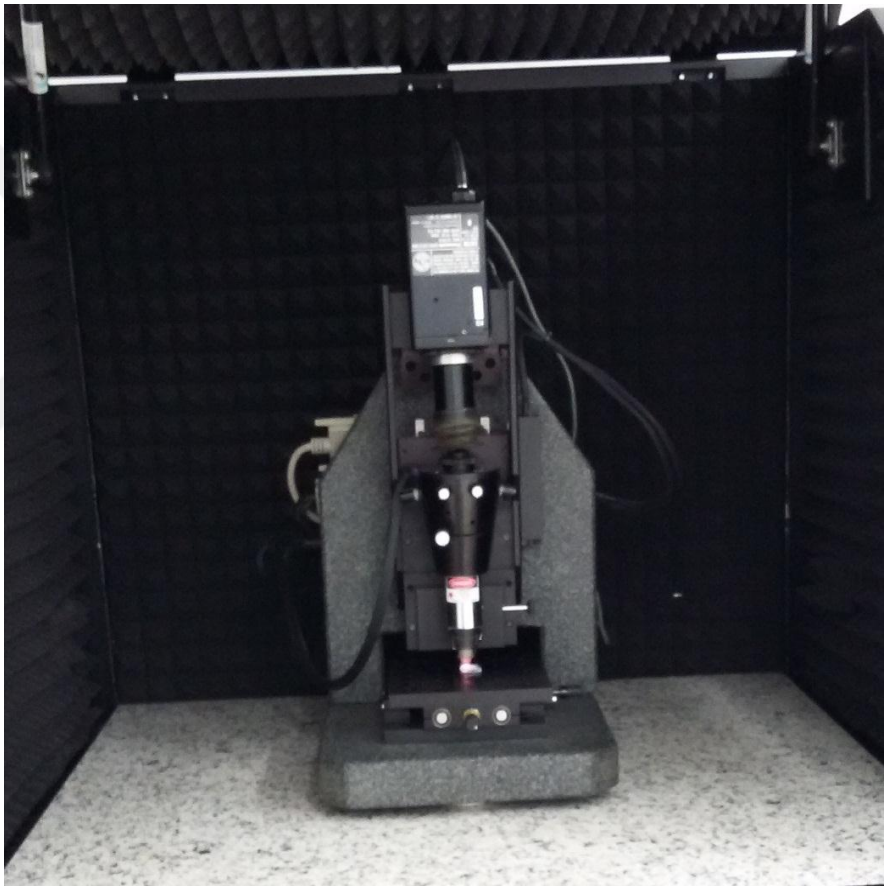


Figure 4.5 Quesant Ambious Q-scope series AFM

4.5 Thickness measurements

An optical profilometer measures the thickness of opaque films thanks to extracted Angstrom-level height difference data from a 3D surface map [42]. In this schema, light is sent to the sample surface, and a reference mirror separates the light beam into two beams as depicted in Fig. 4.6. Constructive and destructive planes exhibit

different responses in an image. In this study, a MicroXAM - 100 Non-Contact Optical Profiler from KLA Tencor shown in Fig. 4.7, was used to determine the thickness of the samples.

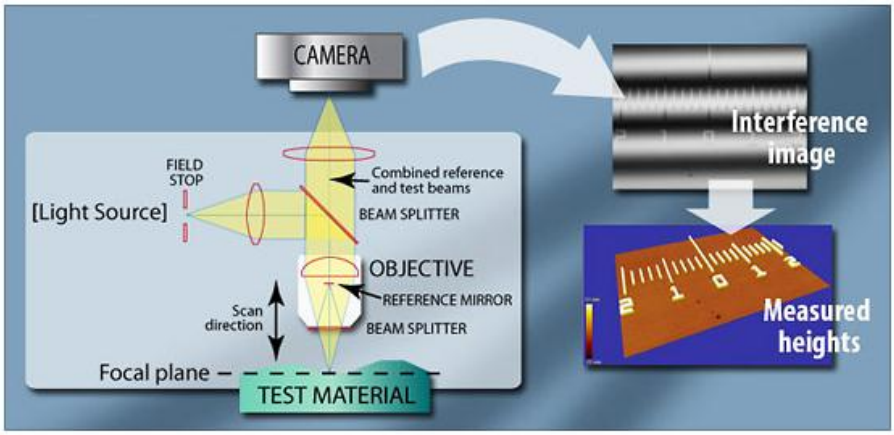


Figure 4.6 Optical profilometer working principles [43]

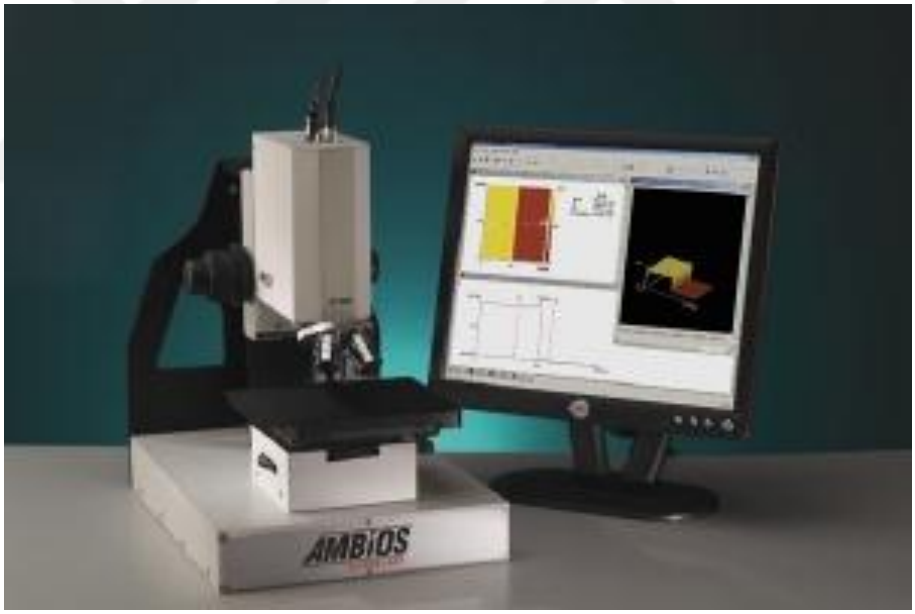


Figure 4.7 Optical profilometer working principles [44]

4.6 Quantum efficiency measurements

The quantum efficiency (QE) value of the solar cell indicates how much current the cell will produce under illumination for a specific wavelength [45]. Typical equipment used to measure QE can be seen in Fig. 4.8. QE measurements are divided into two groups, internal and external quantum efficiencies, denoted IQE and EQE. IQE relates to generated electron-hole pairs as a ratio of adsorbed photons. EQE

scrutinizes how many electron-hole pairs are generated at the ratio of the number of charge carriers collected by the solar cell to the number of photons of a given energy. The relationship between IQE and EQE can be given as follows:

$$IQE = \frac{EQE}{1 - R} \tag{3.2}$$

where R represents the reflectance value. In this study, EQE measurements were done using an Enlitech QE-R (DC mode for DSSCs) measurement system, as shown in Fig. 4.9.

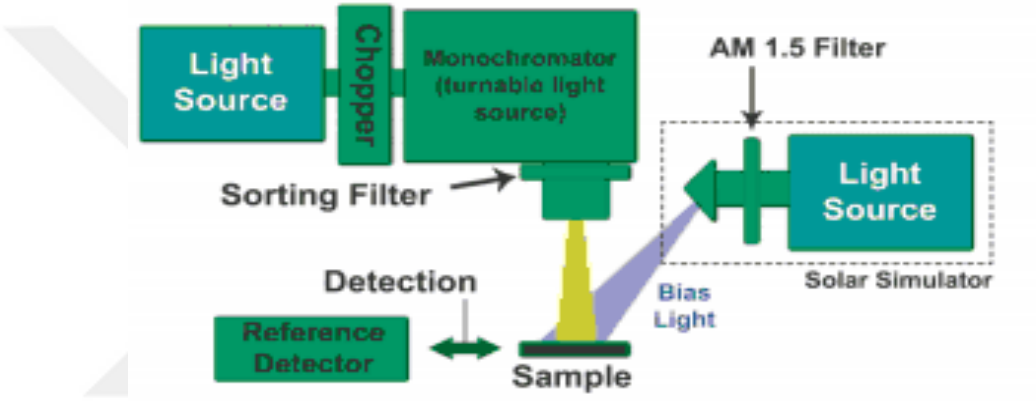


Figure 4.8 Equipment for external quantum efficiency measurements [46]



Figure 4.9 Quantum efficiency measurement system [47]

4.7 Current- voltage measurements

The performance of a solar cell is obtained by considering its ability to convert sunlight into electrical energy and comparing its power with a term called power conversion efficiency. It is basically defined as the ratio of output power of cell and incident light power. The efficiency of a cell can be determined with the following formula,

$$\eta = \frac{P_{out}}{P_{in}} = \frac{V_{oc} * J_{sc} * FF}{P_{in}} * 100 \tag{4.3}$$

where η is the cell power conversion efficiency, P_{out} is generated power from the cell and P_{in} is the power of the incoming light. V_{oc} (V), J_{sc} (mA/cm^2), FF and P_{in} (100 mW/cm^2) terms correspond to open circuit voltage, short circuit current density, fill factor and incident power energy as in Eq. 4.3 , respectively.

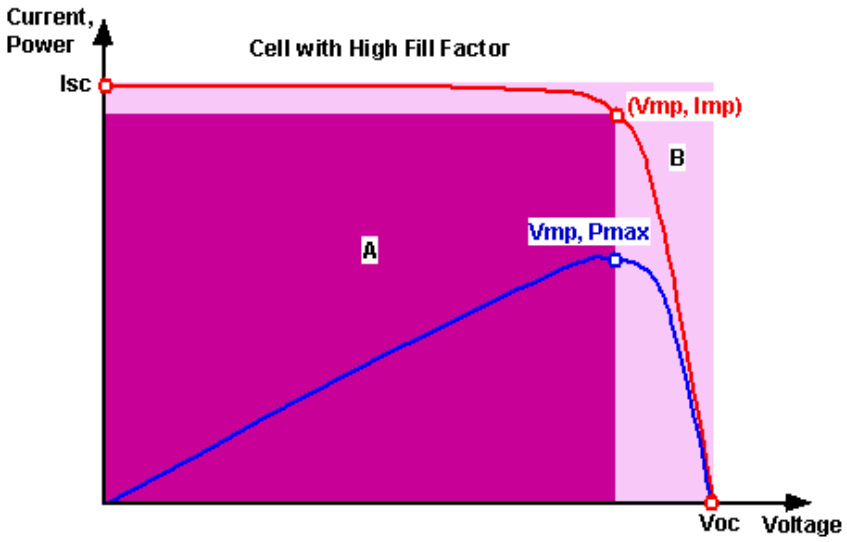


Figure 4.10 Current-voltage curve for solar cells [48]

I_{sc} has the maximum current value when the obtained voltage value is zero. I_{sc} arises via the collection of illumination-generated electrons. It depends on incoming light, number of photons, collection ability, optical properties (absorbance, reflectance) and area of the cell. J_{sc} is obtained by a short circuit current over the active area to eliminate the effect of the area while comparing current performances.

V_{oc} has the maximum voltage value for a cell under open circuit conditions when the net current of the cell is zero. V_{oc} can be determined as a function of band gap energy (E_g).

Fill factor depends on the available current and voltage extracted from the solar cell. For high cell performance, a high value of *FF* is desired. It can be extracted from Eq. 4.4 as a ratio of maximum current times maximum voltage over short circuit current times open circuit voltage.

$$FF = \frac{I_{mp} * V_{mp}}{I_{sc} * V_{oc}} \tag{4.4}$$

For a fair standard comparison, measurements should be performed under standard test conditions. Standard test conditions indicate 1000 W/m^2 incoming radiance at 25 ˚C and this corresponds to 1 sun illumination.

In this study, current-voltage *(I - V)* curve measurements were performed using a Keithley 4200 sourcemeter under 0.3 sun illumination by applying external potential bias and measuring photo-generated current values.

CHAPTER 5

RESULTS AND DISCUSSION

In this section, the properties of the prepared solar cells were investigated by various instruments. Through these tools, morphological, and optical properties, as well as device performance under illumination were obtained and discussed in terms of the contribution of each pre- and post- treatment layer separately.

5.1 XRD results

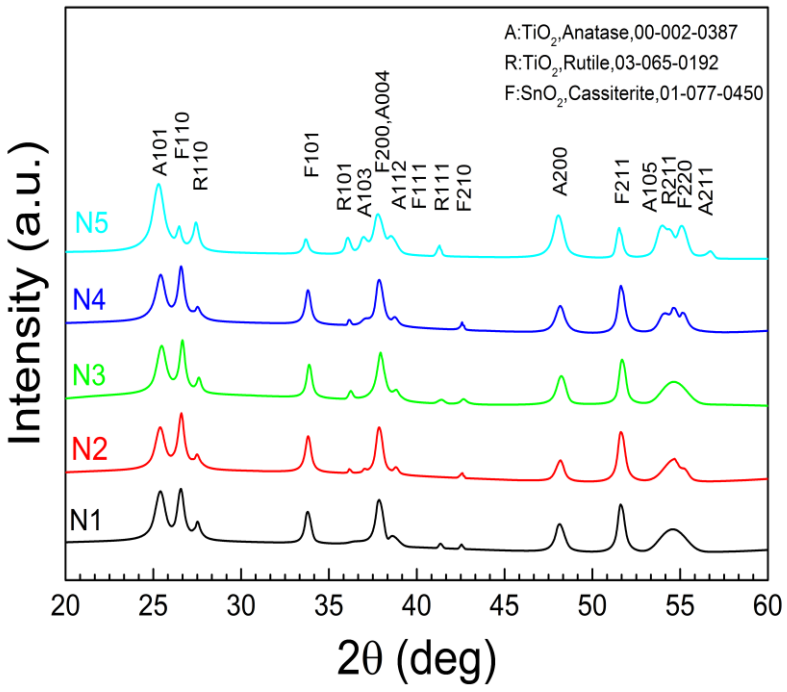


Figure 5.1 XRD patterns of the samples

The XRD pattern gives an idea about phase purity and crystal structure of the samples as shown in Fig. 5.1. The anatase peak located at about 25.35˚ corresponds to (101) orientation and its sharpness has an ascending trend from the sample N1 to N5. Rutile peak located at about 27. 2˚ belongs to the (110) orientation. All diffraction peaks for the samples are in accordance with JSPDS database cards (00-002-0387, 03-065-0192 and 01-077-0450) for both TiO_2 and FTO.

Grain sizes of the samples were extracted using Sherrer's formula (Eq. 5.1) for anatase (101) peak.

Corresponding intensity values for anatase (101) and rutile (110) orientation were represented by I_A and I_R , and the weight percentage of anatase paste was also estimated by using Eq. 5.2. [49]. The results are listed in Table 5.1.

$$D = \frac{0.9\lambda}{\beta cos\theta} \tag{5.1}$$

$$W_A = \frac{1}{(1 + \frac{1.26\, I_R}{I_A})} \tag{5.2}$$

Table 5.1 Grain size and anatase weight percentage values for the samples

Sample #	A101 peak Grain size (nm)	Weight of Anatase
N1	16.2	0.76
N2	20.3	0.75
N3	20.3	0.77
N4	20.6	0.77
N5	20.0	0.83

5.2 Optical profilometer results

By using optical profilometer, thickness values of working electrodes of the samples were measured as 10.8, 10.1, 11.1, 12.7, 23.4 μm, for N1, N2, N3, N4 and N5, respectively. Using a rough calculation it could be said that applying of TiO_2^* ($TiCl_4$) reduces the thickness (N1→N2). However thickness was increased by almost 1 μm with 5-cycle coated layer of TiO_2^{**} (TTIP) (N2→N3). By applying 3 drops of top TiO_2^{***} treatment, thickness was increased by 1.6 μm (N3→N4). Finally, applying the viscous TiO_2 paste and further TiO_2^{***} (TTIP) post treatment resulted in a considerable increase in the thickness (N4→N5). Consequently, by addition of each treatment layer, the thicknesses of the samples were generally increased except from N1→N2. This slight decrease for the sample N2 might have been due to corrosion of the FTO coated glass by acidic $TiCl_4$ treatment. Viscosity also plays an important

role in the thickness. For instance, the thickness range of the application of the TTIP sol is in level of nm, while it is in μm for the viscous TiO2 paste.

5.3 Atomic force microscopy results

Fig. 5.2 shows 2D and 3D topographical AFM pictures of the samples. AFM provides information on the morphological properties of the samples. Root mean square (RMS) values were estimated from AFM measurements, as shown in Table 5.2. Roughness affects light harvesting properties and the performance of solar cells.

After, adding TiO_2^* ($TiCl_4$) layer, (N1→N2) the RMS value was increased. By introducing spin-coated TiO_2^{**} (TTIP) layer, the RMS value was increased (N2→N3). In contrast, when adding TiO_2^{***} (TTIP) (N3→N4) the RMS value was decreased due to the size of the particles. For N5, similar to N4, it also decreased (N4→N5). A high value of RMS is generally desired because of less reflectivity of incoming light. In Table 5.2 the RMS values vary between 27.8 and 57.86 nm for the samples.

Table 5.2 AFM results for the samples

Sample	N1	N2	N3	N4	N5
RMS (nm)	27.84	40.22	57.86	44.44	43.61

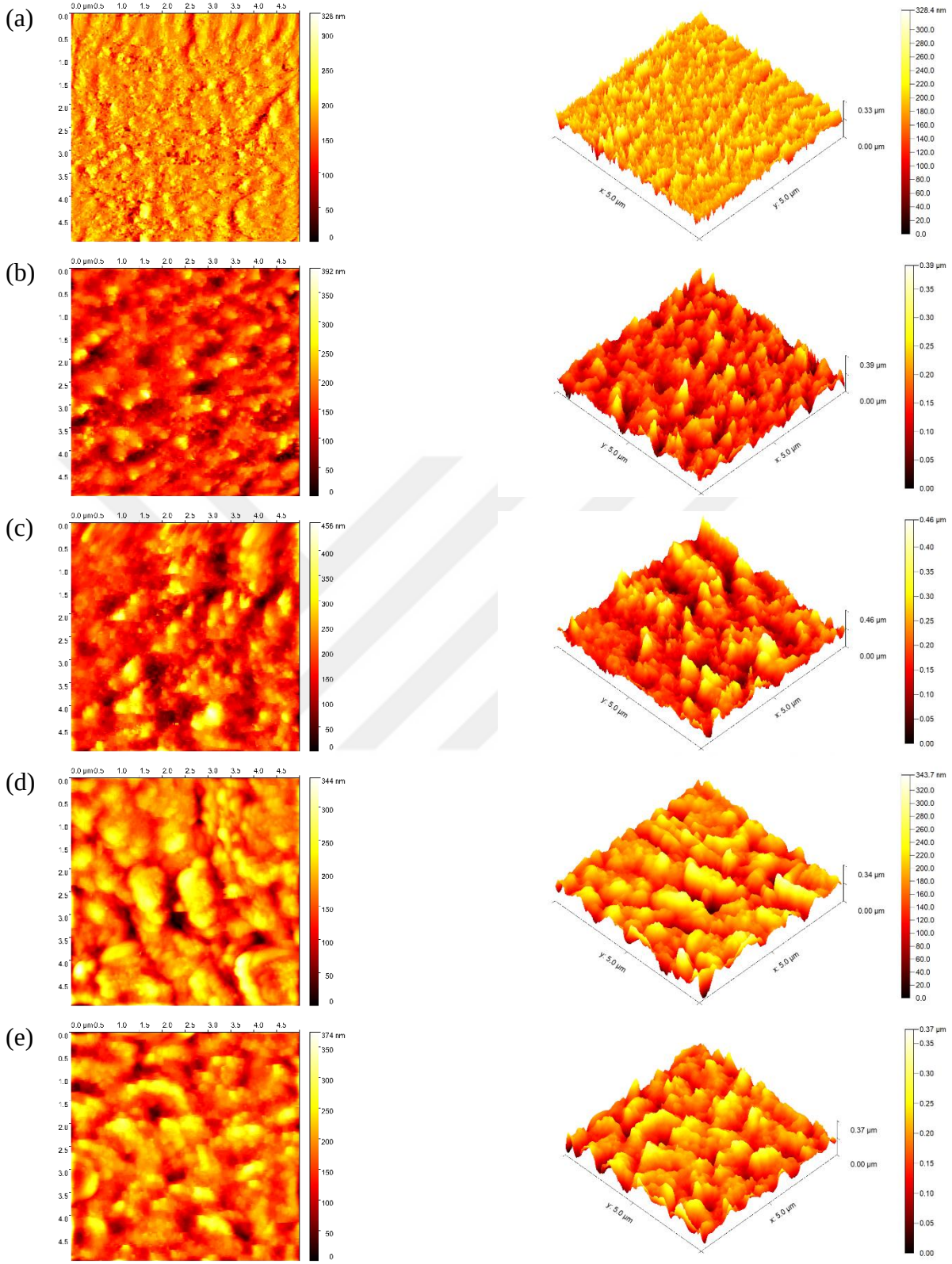


Figure 5.2 2D and 3D topographical AFM pictures of samples (a) N1, (b) N2, (c) N3, (d) N4, (e) N5.

5.4 EQE results

Quantum efficiency measurements were done to analyze how many incident photons can be converted into pairs of charge carriers as a percentage, as represented in Fig 5.3. There was an enhancing trend for the samples when going from N1 to N5, between 300 nm and 800 nm. Even though the region where peaks were observed changed due to particle size, the general trend was reasonable. In order to notice the effect of an additional layer on the EQE, subtraction of values of EQE for the samples was displayed in Fig. 5.4. The contribution of the TiO_2^* ($TiCl_4$)layer over EQE slightly increased in UV and visible regions. In the TiO_2^* ($TiCl_4$) and TiO_2^{**} (TTIP) multi compact layered sample, N3, EQE displayed an enhancement especially in the UV region, even though it was similar to the EQE in the previous sample, N2, in the visible region. When applying a post-TiO_2^{***} (TTIP) treatment, an improvement was observed for all regions. For the thickest sample, N5, EQE was broadened and slightly increased.

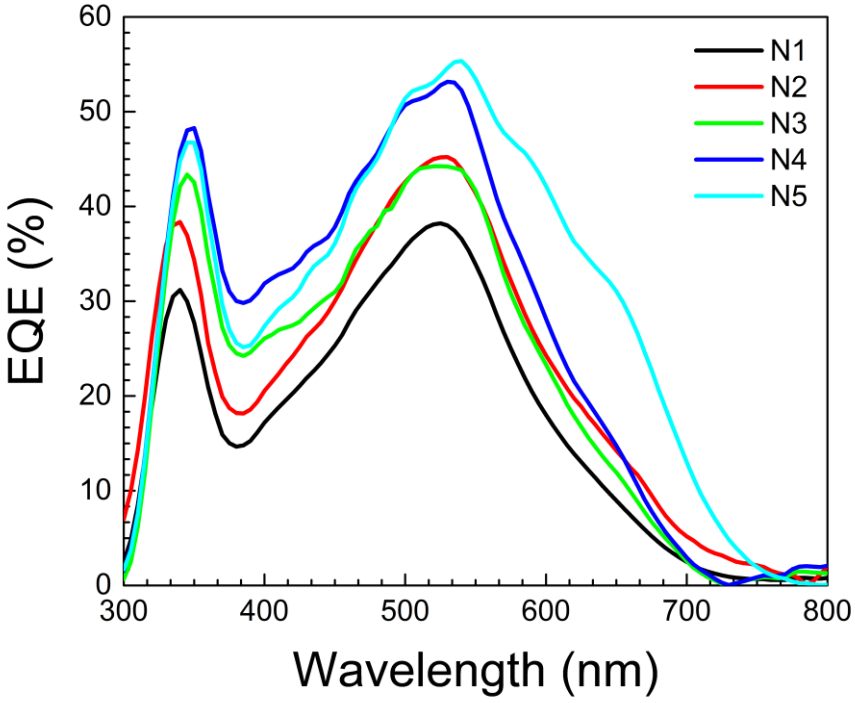


Figure 5.3 External quantum efficiency of the investigated DSSCs

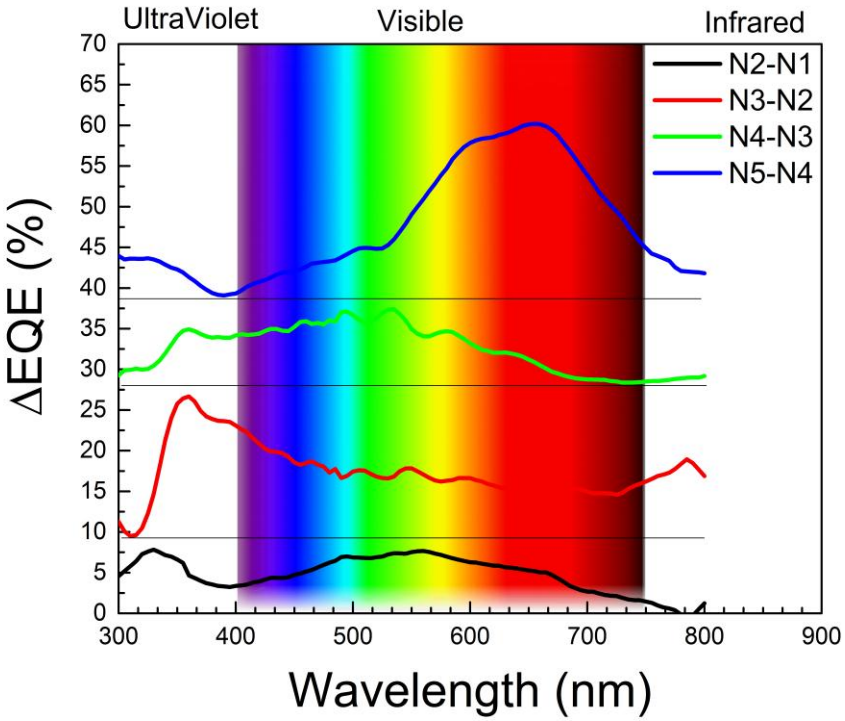
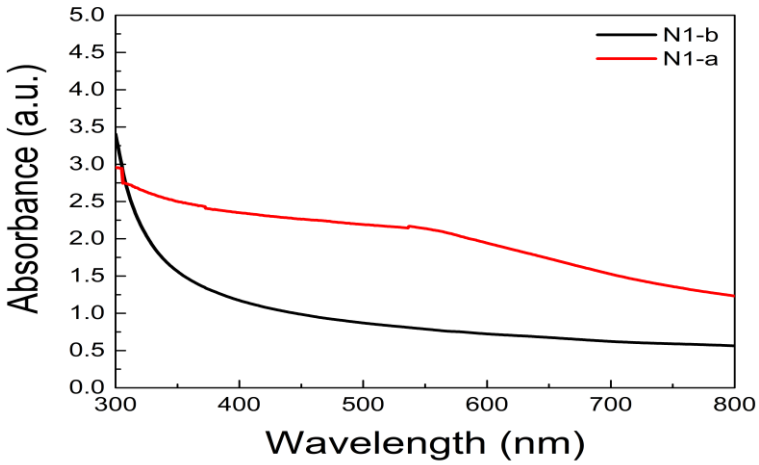


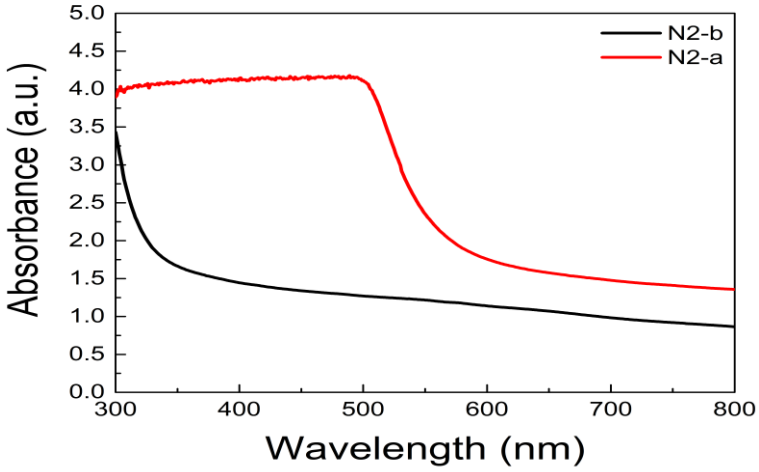
Figure 5.4 Layer-by-layer improvement of EQE

5.5 UV-VIS-NIR results

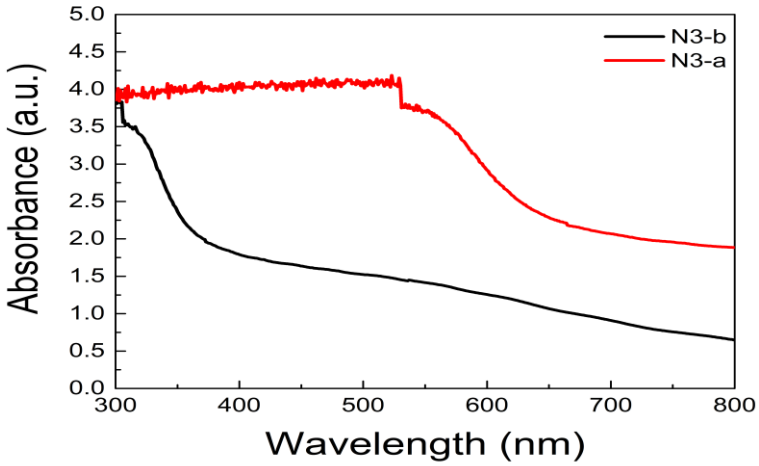
The UV-VIS-NIR absorption spectrum of the samples was measured in the visible range. Fig. 5.5 depicts absorbance versus wavelength for the samples. In the figures, "a" and "b" stand for the cases before and after dye loading, respectively. After dye loading, the addition of dye molecules attached to TiO_2 resulted in a considerable increase in the absorption of sunlight in the visible region for all samples.



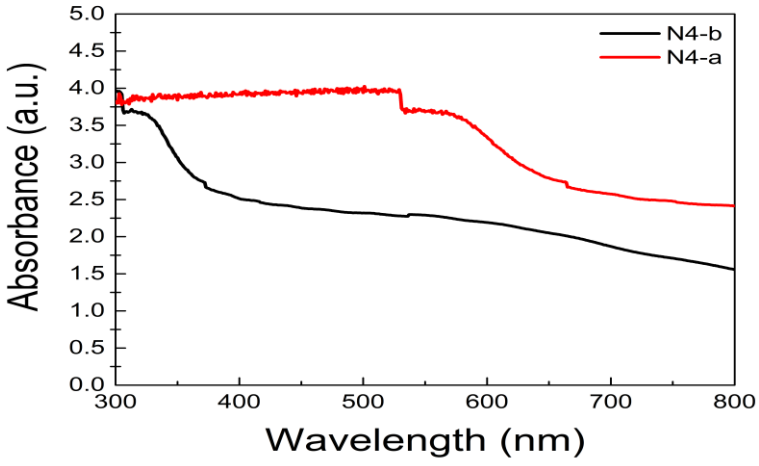
(a)


N2-b
N2-a
Absorbance (a.u.)
Wavelength (nm)
0.0
0.5
1.0
1.5
2.0
2.5
3.0
3.5
4.0
4.5
5.0
300
400
500
600
700
800

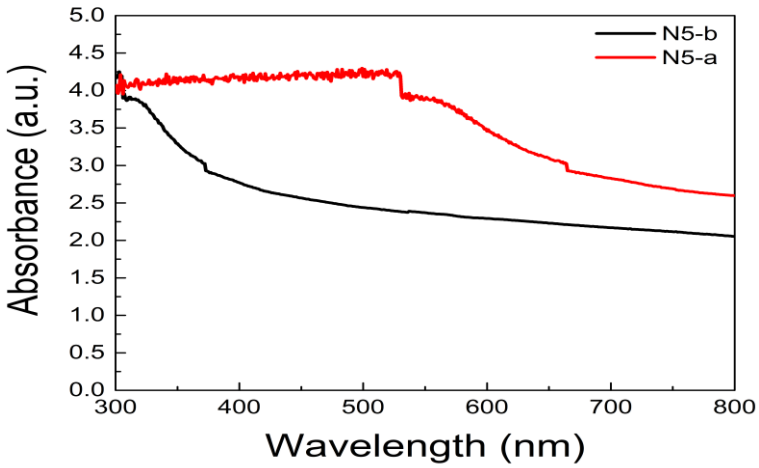
(b)


N3-b
N3-a
Absorbance (a.u.)
Wavelength (nm)
0.0
0.5
1.0
1.5
2.0
2.5
3.0
3.5
4.0
4.5
5.0
300
400
500
600
700
800

(c)


N4-b
N4-a
Absorbance (a.u.)
Wavelength (nm)
0.0
0.5
1.0
1.5
2.0
2.5
3.0
3.5
4.0
4.5
5.0
300
400
500
600
700
800

(d)



(e)

Figure 5.5 Absorbance spectrum of the samples before and after dye loading for (a) N1, (b) N2, (c) N3, (d) N4, (e) N5

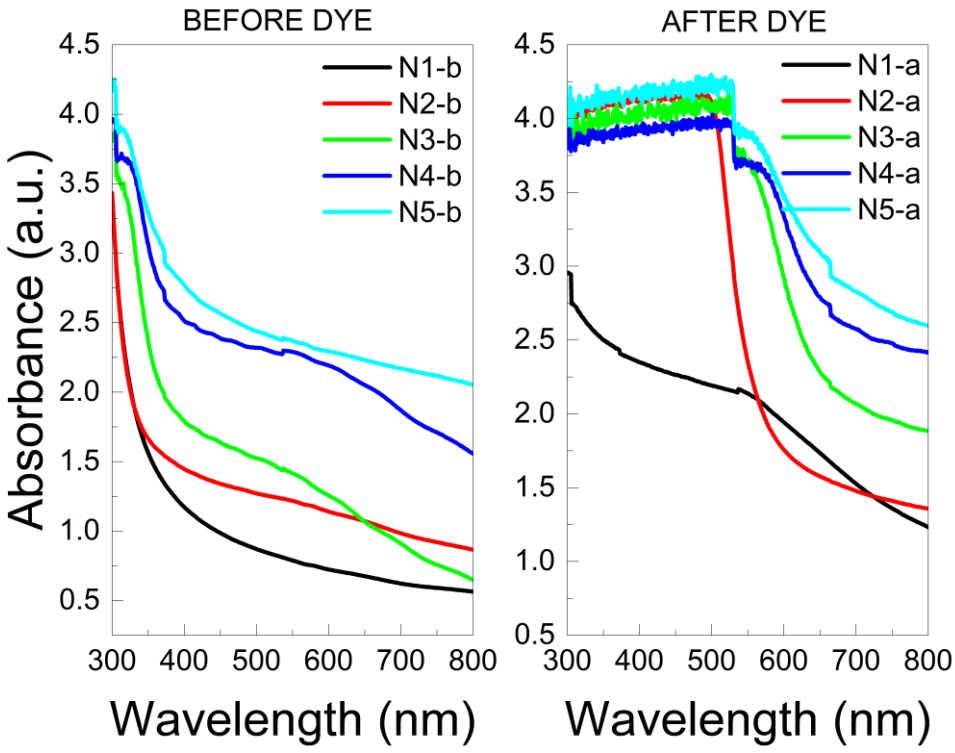
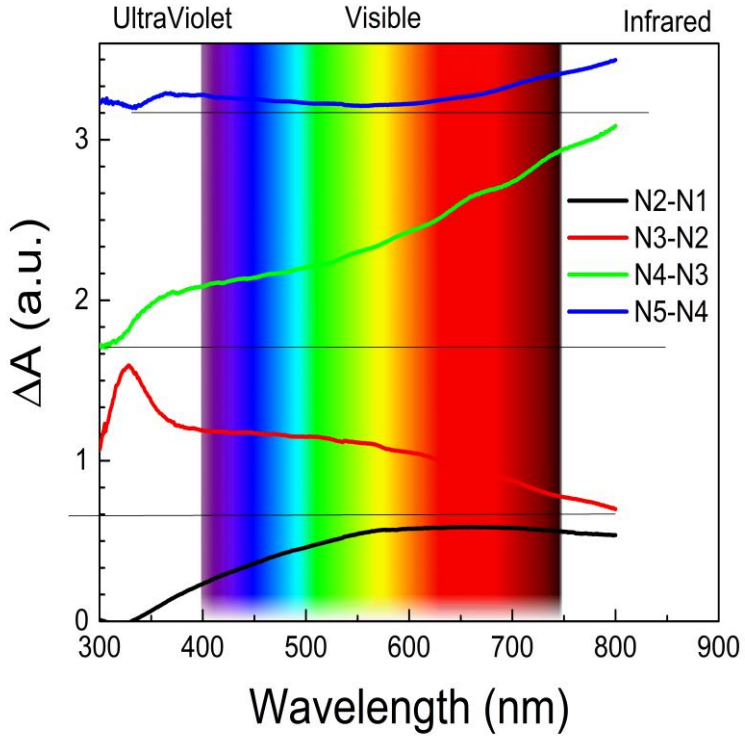
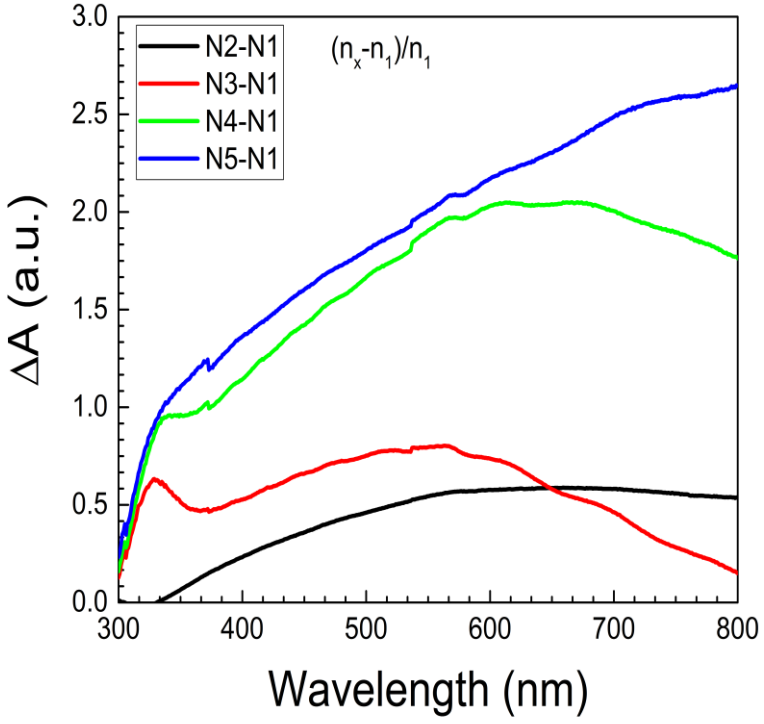


Figure 5.6 Absorbance spectrum of the all samples



(a)



(b)

Figure 5.7 (a) Layer-by-layer and (b) cumulative enhancement of absorbance before dye

Fig. 5.6 shows the development of photoanode absorbance values in the range 300-800 nm. In Fig. 5.7, the individual (a) and cumulative (b) effect of each added layer were examined in more detail. Here, ΔA represents the change in absorbance caused by adding a new layer. Increasing of absorbance by adding layers generally causes an increase in thickness. This can be explained by the TiO_2 framework adsorbing more dye molecules. Similar trends were reported by Tsai et *al*. [50].

If the absorbance value of the first sample is taken as the reference, absorption is improved in the visible and infrared region for N2, as shown in Fig. 5.7.a. For N3, a compact TiO_2^{**} (TTIP) barrier layer was applied in five cycles, the absorption increased again, especially in the UV and visible regions. Light absorption was improved in all regions for N4, which was treated by post-TTIP sol. In addition, this results can be said to be mainly responsible for the cumulative development shown in Fig. 5.7.b. N1 absorbance spectrum was selected as a reference for all subtraction transactions to calculate cumulative change, and the delta of the absorbance spectrum was obtained by dividing results by those to N1. With the effect of increased thickness, a high value of the absorption in the infrared region was obtained for N5.

5.6 Results of current-voltage measurements

To investigate the photovoltaic performance of the fabricated DSSCs with different multilayer structures, the current-voltage (*J-V*) characteristics were obtained under irradiation of 0.3 sun intensity (at 30 mW/cm^2) and are shown in Fig. 5.8. The values of J_{sc}, V_{oc}, *FF* and η of the five solar cells were obtained as plotted in Fig. 5.9. The photovoltaic performance of the cells was also summarized in Table 5.3. The addition of different layers leads to a considerable change in all photovoltaic parameters, i.e., J_{sc}, V_{oc}, *FF* and η. An obvious trend of improvement in the performance of the cells with the increase in J_{sc} was observed by moving from N1 to N5. The cells exhibited a higher short circuit current, but a lower open circuit voltage compared to the bare sample (N1). The most efficient DSSC, based on the configuration of N4 exhibited a J_{SC} of 7.11 mA/cm^2, V_{OC} of 0.63 V, *FF* of 56 % and power conversion efficiency (η) of 8.43 %.

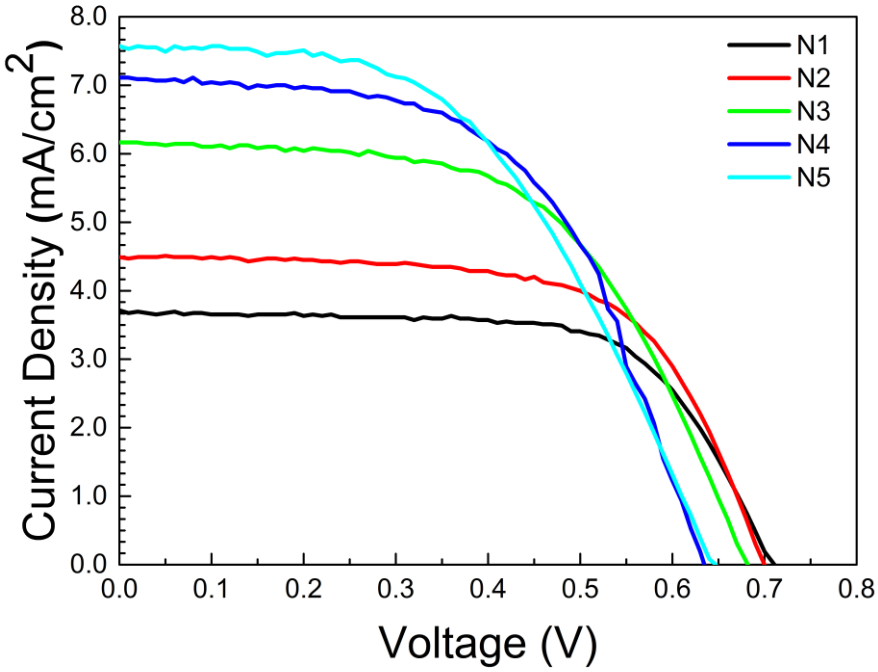


Figure 5.8 J-V results for the samples

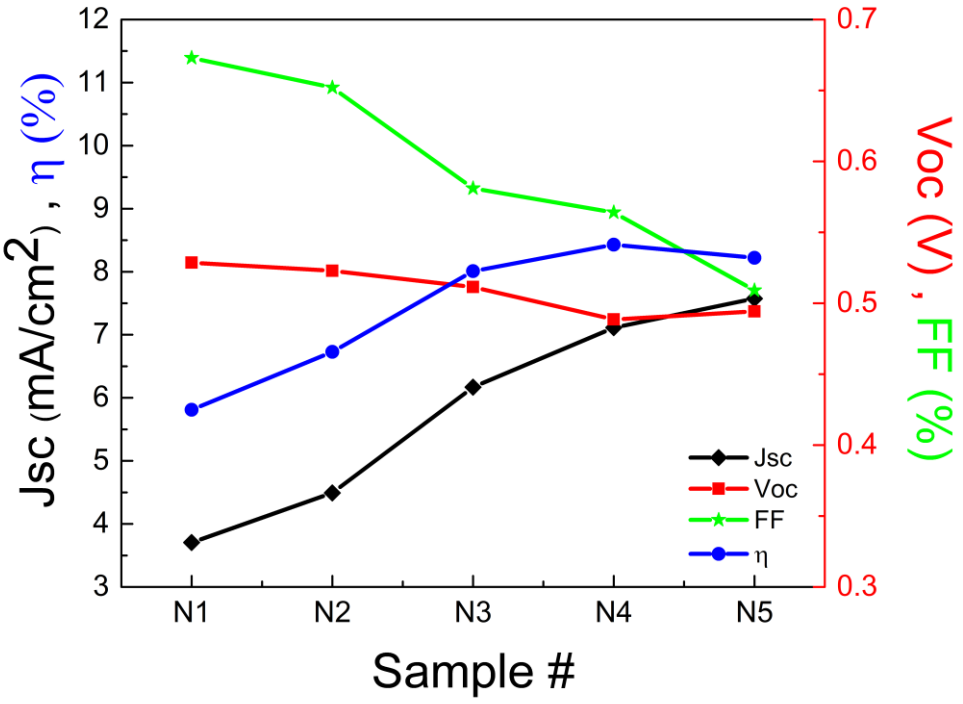


Figure 5.9 Change in external performance parameters

Table 5.3 External parameters of the investigated DSSCs

Sample	J_{sc}(mA/cm^2)	V_{oc} (V)	FF	Ƞ(%)
N1	3.71	0.70	0.67	5.81
N2	4.49	0.69	0.65	6.73
N3	6.17	0.67	0.58	8.01
N4	7.11	0.63	0.56	8.43
N5	7.57	0.64	0.51	8.22

5.7 Discussion of results

The findings indicate that the structure of the photoanode strongly affects performance of the cells. From Table 5.3, one can notice that V_{oc} slightly decreases from 0.7 V for N1 to 0.69 V for N2, while J_{sc} significantly increases from 3.71 mA/cm^2 for N1 to 4.49 mA/cm^2 for N2. This is mainly caused by the reduced back electron recombination, and inhibition of a direct contact between FTO and the electrolyte by the insertion of the TiO_2^* ($TiCl_4$) layer. The presence of this layer leads to an increase in the life time of electrons [25], which produces an increase in J_{sc}. Moreover, reducing recombination could lead to lower saturation current, which would result in a higher V_{oc}. This is not the case for our cells. The slight decrease in V_{oc} can be ascribed to the change in the difference between the quasi Fermi energy levels of TiO_2 and Fermi energy level of the redox electrolyte [51]. A similar trend was previously reported Park et *al.* [25].

To explore the effect of the spin-coated TiO_2^{**} (TTIP) compact barrier layer on performance of the cell, N3 was examined. When the TiO_2^{**} compact barrier layer is deposited on the $TiCI_4$ layer, J_{sc} and η are enhanced when incorporating TiO_2^{**} as the compact layer. The cell exhibits an increased J_{sc} of 6.17 mA/cm^2, a V_{oc} of 0.67 V, and a *FF* of 0.58, and yields an improved η of 8.01 %. In comparison with N2, the enhancement in J_{sc} can be attributed to an improvement in inhibition of back recombination due to increasing blocking layer thickness. This observation is consistent with that reported by Hart et *al.* [52] . Note that N3 is thicker than N2. For N3, a drop in V_{oc} can be expected because of the recombination of migrated charges and transport limitations in the thicker film [53]. It is also noteworthy that the series resistance of the thicker photoanode is larger because the redox species and electrons

move in a long transport length to complete the circuit [53], which leads to a remarkable decrement in *FF*.

To enhance optical absorption and conversion efficiency, the top coating of TiO_2^{***} (TTIP) was introduced. The morphological characteristics of the photoanode are altered by applying a top layer [54]. This treatment helps to fill some pores in mesoporous TiO_2 paste (P25), giving an increase in short circuit current with enhanced electron transport. This layer might behave as a light-scattering layer, which suggests that there may be additional optical phenomena that enhance the light trapping efficiency [55]. Compared with N3, the photoanode became slightly thicker in N4. This thickness falls into the optimum range of 10-14 μm for ruthenium-loaded DSSCs [56]. It allows a large amount of dye-loading and enhances charge collection efficiency with an optimum transport length of migrated carriers. The overall conversion efficiency of N4 was 1.45 times superior to that of the bare cell (N1), leading to a possibility of achieving 8.43 % efficiency under without having to reduce fundamental energy losses.

Finally, the repeating sequence of TTIP/P25 layers was introduced (see N5). It was not an efficient approach with which to further boost the performance of the cell due to having a considerably thick photoanode layer. Slightly less conversion efficiency was observed for N5 (8.22 %). Introducing new TTIP/P25 layers remarkably increases the thickness of the photoanode. Such a significant increase in the thickness degrades the performance of the device since the electron transport length becomes long, leading to an increase in the probability of recombination [57].

In conclusion, multilayer dye-sensitized solar cells have experimentally been demonstrated to have a power conversion efficiency up to 8.43 %. The high efficiency of our best solar cell (N4) can be ascribed to the effective electron transport length, charge collection efficiency, and the photoanode's absorption ability.

REFERENCES

[1] K. Kalyanasundaram, DYE-SENSITIZED SOLAR CELLS, Lausanne: EPFL Press, 2010.

[2] A. Smee, in *Elements of Electro-biology, Or the Voltaic Mechanism of Man of Electro-pathology, Especially of the Nervous System and of Electro-therapeutics.*, 1849, p. 108.

[3] T. E. o. E. Britannica, "Encyclopædia Britannica," Retrived October 11, 2017 from https://www.britannica.com/science/photoelectric-effect.

[4] "nobelprize.org," Retrived October 11, 2017 from https://www.nobelprize.org/nobel_prizes/physics/laureates/1921/.

[5] M. G. Brian O'Regan, "A low-cost, high-efficiency solar cell based on dye-sensitized colloidal TiO2 films," *Nature* , no. 353, p. 737–740, 1991.

[6] J. Lee, J. B., J. S., Y. Y., P. S., K. J., K. Y., J. Y. and K. M., "Multi-layered TiO2 nanostructured films for dye-sensitizeed solar cells," *J Mater Sci:Mater Electron*, no. 20, pp. 446-450, 2009.

[7] B. A. Gregg, "The Photoconversion Mechansim of Excitonic Solar Cells," *MRS Bulletin*, no. 30, pp. 20-22, 2005.

[8] Y. Xu, . T. Gong and . J. N. Munday, "The generalized Shockley-Queisser limit for nanostructured solar cells," *Nature, Scientific Reports* , no. 5, 2015.

[9] "https://www.aerosil.com/," Retrived December 1, 2017 from https://www.aerosil.com/product/aerosil/en/industries/electronics/dye-sensitized-solar-cells/pages/default.aspx.

[10] "http://www.elp.uji.es/," Retrived December 1, 2017 from http://www.elp.uji.es/juan_home/images/solar_cell/DSSCredox.jpg.

[11] K. Badeker, *Annals of Physics* , no. 22, p. 749, 1907.

[12] TECHINSTRO, "TECHINSTRO," Retrived October 20, 2017 from https://www.techinstro.com/difference-ito-fto-coated-glass/.

[13] S. Suhaimi, M. M. Shahimin, Z. Alahmed, . J. Chyský and A. H. Reshak, "Materials for Enhanced Dye-Sensitized Solar Cell Performance:Electrochemical Application," *International Journal of Electrochemical Science*, no. 10, pp. 2859-2871, 2015.

[14] S. P. P. A. L. H. N. R. R. &. H. N. M. Lim, "Boosting Photovoltaic Performance of Dye-Sensitized Solar Cells Using Silver Nanoparticle-Decorated N,S-Co-Doped-TiO2 Photoanode," *Scientific Reports*, vol. 5, no.

11922, 2015.

[15] G. Li, C. P. Richter, R. L. Milot, L. Cai and C. A. Schmuttenmaer, "Synergistic effect between anatase and rutile TiO2 nanoparticles in dye-sensitized solar cells," *Dalton Transactions,* no. 45, p. 10078–10085, 2009.

[16] P. A. R. N. A. Ahmad M.S., "Advancedments in the development of TiO2 photoanodes and its fabrication methods for DSSC applications. A Review," *Renewable and Sustainable Energy Reviews,* no. 77, pp. 89-108, 2017.

[17] F.-L. C. A. T. A. R.-C. J. Navas J., "Improving open-circuit voltage in DSSCs using Cu-doped TiO2 as a semiconductor," *Physica Status Solidi A,* no. 2, pp. 378-385, 2012.

[18] "http://www.dianliwenmi.com/," Retrived December 22, 2017 from http://www.dianliwenmi.com/postimg_4636545.html.

[19] "National Instruments," Retrived December 1, 2017 from http://www.ni.com/white-paper/7230/en/.

[20] "http://www.yorku.ca," Retrived December 1, 2017 from http://www.yorku.ca/planters/photosynthesis/2014_08_15_lab_manual_static_html/index.html.

[21] O. Jesse W. and H. Thomas W., "Recombination and redox couples in dye-sensitized solar cells," *Coordination Chemistry Reviews,* no. 257 , p. 1533–1543, 2013.

[22] "https://ecee.colorado.edu/~," Retrived December 22, 2017 from https://ecee.colorado.edu/~bart/book/book/chapter2/ch2_8.htm.

[23] "https://photon.libretexts.org," Retrived December 5, 2017 from https://photon.libretexts.org/The_Science_of_Solar/Solar_Basics/C._Semiconductors_and_Solar_Interactions/IV._Recombination_of_Charge_Carriers/3._Auger_Recombination.

[24] S. Arman and M. H. Nourmohammadi, "Influence of TiO2 Electrode Properties on Performance of Dye-Sensitized Solar Cells," *International Journal of Electrochemical Science,* no. 7, pp. 12078 - 12089, 2012.

[25] J. Park and M. Lee, "Performance Enhancement of Dye-Sensitized Solar Cell wiith a TiCL4-Treated TiO2 Compact Layer," *Electron Mater. Lett.,* vol. 11, no. 2, pp. 271-275, 2015.

[26] Y. Lu-Ting, W. Fang-Lu, P. Lan, Z. Li-Juan, L. Pu-Jun, D. Sui-Yang and L. Tian-Xiang, "Photoanode of Dye-Sensitized Solar Cells Based on a ZnO/TiO2 Composite Film," *Hindawi, International Journal of Photoenergy,* no. 2012, p.

4, 2012.

[27] J. Ming-Jer, W. Yi-Lun, C. Liann-Be and C. Lee, "Particle Size Effects of TiO2 Layers on the Solar Efficiency of Dye-Sensitized Solar Cells," *International Journal of Photoenergy,* no. 2013, p. 9, 2013.

[28] Y. Hua, Z. Shanqing, Z. Huijun, X. Bofei, L. Porun and W. Geoffrey, "High-Performance TiO2 Photoanode with an Efficient Electron Transport Network for Dye-Sensitized Solar Cells," *J. Phys. Chem. ,* no. 113, p. 16277–16282, 2009.

[29] P. Mengmei, H. Niu, Z. Xingzhong, F. Jun and Z. Xiaoli, "Enhanced Efficiency of Dye Sensitized Solar Cell by High Surface Area Anatase-TiO2 Modified P25 Paste," *Journal of Nanomaterials,* no. 2013, 2013.

[30] A. Kontos , A. Kontos , D. Tsoukleris, M. Bernard , N. Spyrellis and P. Falaras, "Nanostructured TiO2 films for DSSCS prepared by combining doctor-blade and sol–gel techniques," *Journal of Materials Processing Technology,* Vols. 1-3, no. 196, pp. 243-248, 2008.

[31] K. Zouhour, K. Moufida Ben, A. Tarek and G. Rached, "Effect of TiO2 blocking layer synthesised by a sol–gel method in performances of fluorine-doped tin oxide/TiO2/dyed-TiO2/electrolyte/pt/fluorine-doped tin oxide solar cells based on natural mallow dye," *Micro & Nano Letters,* vol. 2, no. 11, p. 94–98, 2015.

[32] Z. Wang , K. Sayama and H. Sugihara, "Efficient eosin y dye-sensitized solar cell containing Br-/Br3- electrolyte," *J Phys Chem B.,* no. 109(47), pp. 22449-22455, 2005.

[33] Ting-Chien, LiuChih-Chung, WuChih-Hsiang, Huang and C.-M. Chen, "Effects of Ethyl Cellulose on Performance of Titania Photoanode for Dye-sensitized Solar Cells," *Journal of Electronic Materials,* vol. 12, no. 45, p. 6192–6199, 2016.

[34] S. Ito, T. . N. Murakami, P. Comte, P. Liska, C. Grätzel, M. K. Nazeeruddin and M. Grätzel, "Fabrication of thin film dye sensitized solar cells with solar to electric power conversion efficiency over 10%," *Thin Solid Films ,* no. 516, p. 4613–4619, 2008.

[35] H. Choi , C. Nahm , J. Kim, J. Moon , S. Nam, D. Jung and B. Park , "The effect ofTiCl4 treated TiO2 compact layer on the performance of dye-sensitized solar cell," *Current Applied Physics,* no. 12, pp. 737-741, 2012.

[36] S.Tatay, "Solution Processed Spin Electronics," Retrieved December 14 2017 from https://www.slideshare.net/seta667/hints-elfos-forslidesahre.

[37] "https://www.rigaku.com/," Retrived October 10, 2017 from https://www.rigaku.com/en/techniques/xrd.

[38] "prweb," Retrived December 1, 2017 from http://www.prweb.com/releases/2017/06/prweb14384458.htm.

[39] "shimadzu," Retrived January 3, 2018 from https://www.shimadzu.com/an/molecular_spectro/uv/uv-3600plus.html.

[40] "http://www.parkafm.com," Retrived December 5, 2017 from http://www.parkafm.com/index.php/medias/nano-academy/how-afm-works.

[41] Z. Deng, "http://qilerongrong.org/," Retrived December 5, 2017 from http://qilerongrong.org/Pro_Zhao.html.

[42] "http://www.laserfocusworld.com/," [Retrived December 5, 2017 from http://www.laserfocusworld.com/articles/print/volume-46/issue-1/features/optical-surface-profiling.html.

[43] "https://www.zygo.com/," Retrived December 5, 2017 from https://www.zygo.com/?/met/profilers/opticalprofilersabout.htm.

[44] "azooptics.com," Retrived January 3, 2018 from https://www.azooptics.com/optics-equipment-details.aspx?EquipID=52.

[45] "pveducation.org," Retrived December 28, 2017 from http://www.pveducation.org/pvcdrom/quantum-efficiency.

[46] "EQE MEasurement," Retrived December 28, 2017 from http://www.deepphotonicsindia.com/images/product/pts2.png.

[47] Retrived January 3, 2018 from http://www.shin-yu.com.tw/products_(a9).htm.

[48] "www.pveducation.org," Retrived December 28, 2017 from http://www.pveducation.org/pvcdrom/fill-factor-0.

[49] A. Yildiz , N. Serin , M. Kasap , T. Serin and D. Mardare, "The thickness effect on the electrical conduction mechanism in titanium oxide thin films," *Journal of Alloys and Compounds,* no. 493, p. 227–232, 2010.

[50] T. Jenn Kai, H. Wen Dung, W. Tian Chiuan, M. Teen Hang and C. Wen Jie, "Effect of compressed TiO2 nanoparticle thin film thickness on the performance of dye-sensitized solar cells," *Nanoscale Res Lett.*, vol. 1, no. 8, p. 459, 2013.

[51] J. Bisquert, Nanostructured Energy Devices; Equilibrium Concepts and Kinetics, CRC Press, 2015.

[52] J. N. Hart, D. Menzies, Y. Cheng, G. P. Simon and L. Spiccia, "TiO2 sol-gel blocking layers for dye sensitized solar cells," *Compes Rendus Chimie,* vol. 9, pp. 622-626, 2006.

[53] Z. Wang, H. Kawauchi, T. Kashima and H. Arakawa , "Significant influence of TiO2 photoelectrode morphology on the energy conversion efficiency of N719 dye-sensitized solar cell," *Coordination Chemistry Reviews,* vol. 248, no. 13-14, pp. 1381-1389, 2004.

[54] K. Basu, D. Benetti, H. Zhao, L. Jin , F. Vetrone , A. Vomiero and F. Rosei, "Enhanced photovoltaic properties in dye-sensitized solar cells by surface treatment of SnO2 photoanodes," Nature Scientific Reports, 2016.

[55] Z. Sun, J. Kim, Y. Zhao, F. Bijarbooneh and V. Malgras, "Improved photovoltaic performance of dyesensitized solar cells with modified self-assembling," *Journal of Materials Chemistry,* vol. 22, no. 23, pp. 11711-11719, 2012.

[56] T. Morimoto, N. Fujikawa, Y. Ogomi, S. Pandey and S. Hayase , "Parametric Optimization of Experimental Conditions for Dye-Sensitized Solar Cells based on Far-red Sensitive Squaraine Dye," *Journal of Physics: Conference Series,* vol. 704, no. 012002, 2016.

[57] J. Tsai, W. Hsu, T. Wu, T. Meen and W. Chong, "Effect of compressed TiO2 nanoparticle thin film thickness on the performance of dye-sensitized solar cells," *Nanoscale Research Letters ,* vol. 8, no. 459, 2013.

[58] R. G.D., H. F.Z., A. R., J. Plessis and X.J.Dai, "Low temperature reactively sputtered crystalline TiO2 thin film as effective blocking layer for perovskite solar cells," *Thin Solid Films,* no. 636, pp. 307-313, 2017.

[59] L. Schmidt-Mende and J. Weickert, Organic & Hybrid Solar Cells, De Gruyter, 2016.

CURRICULUM VITAE



PERSONAL INFORMATION

Name Surname : Aycan ATLI

Date of Birth : 1990

E-mail : aycanatli18@gmail.com

EDUCATION

Bachelor : Anadolu University/ Eskişehir (2008-2012) (2.99/4.0)

Master Degree : Ankara Yıldırım Beyazıt University / (2016-continued)

WORK EXPERIENCE

Research Assist. : Ankara Yıldırım Beyazıt University / (2016-continued)

Türk-Alman University / (2016 March- June)

TOPICS OF INTEREST

Solar cells, Dye sensitized solar cells

PUBLISHED WORKS

(Poster) **A.Atlı,** A.Atılgan, M.Sbeta and A.Yıldız,' Natural and synthetic sensitizer effects on TiO_2 based dye sensitized solar cells', ICSMD17, Konya, August 2017